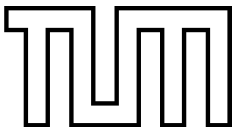

Technische Universität München

Department of Mathematics

A Fast Curvelet Transform for Sparse Reconstruction in Limited Angle Tomography

Master's Thesis by Sebastian Schmelcher

Supervisor: Prof. Dr. Rupert Lasser

Advisor: Dr. Laurent Demaret, Dipl.-Math. Jürgen Frikel

Submission date: October 19th, 2012

I hereby declare that I have written the Master's Thesis on my own and have used no other than the stated sources and aids.

Munich, October 19th 2012

. . . . . .

(Sebastian Schmelcher)

Zusammenfassung

Die *Limited Angle Tomography* ist ein tomographisches Verfahren, bei dem Messdaten eines Patienten oder eines Objektes nicht von allen Seiten, sondern nur aus einem eingeschränkten Winkelbereich heraus erhoben werden. Der Grund für diese Einschränkung des Messbereiches liegt oft darin, empfindliche Strukturen in der Nähe der betrachteten Stelle vor Strahlungseinflüssen zu schützen. Ein Beispiel für solche Strukturen ist der Hirnstamm bei der Tomographie des Kiefers in der Zahnmedizin oder die inneren Organe wie die Lunge in der Mammographie. Die aus diesem Verfahren resultierende Unvollständigkeit der Messdaten im Vergleich zu einer herkömmlichen, kompletten tomographischen Messung führt dazu, dass das betrachtete Rekonstruktionsproblem schlecht gestellt ist. Zusammen mit der Tatsache, dass tomographische Messdaten immer leicht verrauscht sind, liefern übliche Rekonstruktionsmethoden, wie die *Filtered Backprojection* keine zufriedenstellenden Ergebnisse, sondern stark von Artefakten beeinträchtigte Bilder.

Das Ziel dieser Masterarbeit ist die Weiterentwicklung einer Rekonstruktionsmethode in der *Limited Angle Tomography*, die artefaktfrei und unempfindlich in Bezug auf verrauschte Messdaten ist. Unter Verwendung des *Fourier Slice Theorems* kann man anhand der Winkel, zu denen Messdaten existieren, eine Unterteilung der Fourierebene vornehmen: Fourier Koeffizienten innerhalb bestimmter Winkelbereiche des Fourier Raumes können durch die Messungen berechnet werden; Fourier Koeffizienten in den übrigen Bereichen können nicht berechnet werden. Dies motiviert die Verwendung der Curvelet Transformation. Ein grundlegender Aspekt in der Definition dieser Transformation ist die Unterteilung des Fourierraumes in verschiedene Winkelbereiche. Hiermit lassen sich gezielt die Bereiche der Fourierebene von der Rekonstruktion ausschließen, die nicht gemessen wurden. Hierfür werden im Laufe dieser Arbeit mehrere Aufteilungen der Fourierebene entwickelt, die dann für die Definition einer modifizierten Curvelet Transformation verwendet werden. Bei der Aufteilung des Fourier Raumes wird insbesondere auf die Vermeidung von artefakterzeugenden Strukturen, wie harte Kanten zwischen verfügbaren und nicht verfügbaren Koeffizienten, geachtet. Für die entwickelten Aufteilungen wird eine schnelle digitale Curvelet Transformation implementiert.

Anschließend stellen wir mit Hilfe der Curvelet Transformation das Rekonstruktionsproblem auf. Hierbei nutzen wir eine weitere Eigenschaft der Curvelet Transformation: Diese Transformation ist optimal geeignet, um Kanten in Bildern mit wenigen Koeffizienten darzustellen. Dies motiviert die Betrachtung eines Rekonstruktionsproblems, das die Anzahl der nicht nullwertigen Curveletkoeffizienten bestraft.

Schließlich zeigen wir numerische Ergebnisse der Rekonstruktion mit Hilfe der modifizierten Curvelet Transformation und des vorgestellten Rekonstruktionsproblems. Es zeigt sich, dass die entwickelte Rekonstruktionsmethode gut für den Einsatz in der *Limited Angle Tomography* geeignet ist.

Abstract

Limited Angle Tomography is a tomographic procedure, where measurements are not taken from each direction around a patient or an object, but only from within a limited angular range. This limitation of the measurements often is a consequence of protecting sensible structures close by the object that is to be imaged. Typical examples are the brainstem in the tomography of the jaws or the inner organs like the lung in mammography. In comparison to a traditional, full angular scan the data in limited angle tomography is incomplete. This leads to a severe ill-posedness of the considered reconstruction problem. Together with the fact that tomographic measurements always exhibit some noise, conventional reconstruction methods like the filtered backprojection do not yield satisfying results but images that are strongly corrupted by artifacts.

The aim of this master's thesis is the further development of an artifact-free and noise-insensitive reconstruction method in limited angle tomography. We use the Fourier-Slice Theorem in order to subdivide the Fourier plane into angular regions of coefficient that can be computed based on based on the angles that are given by the data acquisition and angular region of the Fourier plane that are uncomputable. This motivates the consideration of the curvelet transform. A basal aspect in the definition of this transform is the tiling of the Fourier plane into different angular scales. With this, the regions of the Fourier plane that are not computable by the measurements can be excluded from reconstruction process. In the course of this thesis we develop different tilings of the Fourier plane that are used for the definition of a modified curvelet transform. We take care of structures in the tilings that cause artifacts, like hard cut-offs at the boundary of measurable and unmeasurable coefficients. For the presented tilings a fast digital curvelet transform is implemented.

Afterwards, we set up the reconstruction problem using the curvelet transform. We use another feature of the curvelet transform: This transform yields an optimal sparse representation of objects with edges. This motivates the consideration of a reconstruction problem that punishes the number of non-zero curvelet coefficients.

Finally, we present the numerical results of our reconstruction method in combination with the modified curvelet transform. It becomes apparent that the developed reconstruction method is well suited for the use in limited angle tomography.

Contents

Introduction

The present thesis is concerned with mathematical methods in medical image processing, in particular computed tomography. Tomography is a common and wide spread tool for medical diagnoses. It is of great benefit to have the possibility to look inside a patient without the hazards of a surgery. Especially in the field of cancer check-ups tomography opens new possibilities. E.g. the detection of small tumors that are not palpable from the outside is one great benefit of this technique. But every tomography based on x-rays naturally involves the risk of causing damage to cells in the body and hence, to the patient. Therefore, in medical imaging it is important to reduce the dose of radiation the patient is exposed to, in order to minimize the risk of causing harm. One possibility to reduce the overall dose, a patient is exposed to, is to perform the single tomographic measurements with less radiation. Unfortunately, a decrease of the radiation level leads to an increasing of the noise level of the measurement data.

Another consequence of the reduction of radiation dose is to take measurements solely of the part of the body that is needed for the considered diagnosis. E.g. in breast tomosynthesis only measurements of the breast and not of the whole upper torso are made. Or even more critical, in dental tomography only the jaws and not he whole head, including the very sensitive brainstem, are radiated during image acquisition. This procedure reduces radiation, but brings along some challenging problems: the considered body part is at least partially surrounded by other body parts that make it physically impossible to take measurements from every direction. As a consequence, in a lot of applications only measurements within a certain angular range are taken. This technique is called Limited Angle tomography. Unfortunately, the exclusion of measurements has a negative influence on the resulting image quality. In limited angle tomography strong artifacts are present. These artifacts can withhold the diagnosis or in the worst case, can lead to misdiagnoses. Nevertheless, this technique is especially interesting in situations, where the acquisition of measurements is physically impossible for all angles around the considered object. Among others, the above mentioned breast tomosynthesis or dental tomography are examples, where the use of limited angle tomography is very common.

Motivated by this medical background, the aim of this thesis is the construction of an artifact-free reconstruction method in limited angle tomography that is capable of handling noise in the measurement data. A reconstruction method with these features is well suited to be used in the described situations and therefore, helps diagnosing a patient with minimal exposure of radiation and hence, minimal risk of causing damage to the patient during image acquisition. To archive this

we organize our thesis in the following way:

We introduce the mathematic background in Chapter 1. Here the data acquisition process is modeled, using the Radon transform. This transform describes the physical situation of the tomographic measurements. We introduce the curvelet Transform, which is powerful in representing objects with edges in a sparse way. This will be used for the sparse reconstruction algorithm introduced afterwards. We finish Chapter 1 by showing typical artifacts that are present in images reconstructed from limited angle tomographic measurements.

Chapter 2 is dedicated to the adaption to the limited angular range. Here we present different methods to adjust the curvelet transform to the use in limited angle tomography. This is done by adjusting the curvelet tiling, the tiling of the Fourier plane that defines the curvelet transform. In particular, artifact reduction is considered at this point.

In Chapter 3 we elaborate a fast discrete version of the curvelet transform. We start with a minimal, straight forward workflow for the curvelet analysis and synthesis algorithm. This algorithm is examined and the occuring problems are handled. In the end, we present a fast digital curvelet transform that is suited for the use in limited angle tomographic reconstruction. To conclude the chapter, we compare our implementation to another implementation of the curvelet transform, that is not optimized for the use in limited angle tomography.

The final algorithm is then used for numerical experiments in Chapter 4. Here, we compare results for different parameter values and work out which parameter values lead to the best results.

Finally, we conclude this thesis by discussing our results in Chapter 5.

1 Curvelets in Limited Angle Tomography

Tomography is concerned with the reconstruction of objects by sectional measurements. An object is radiated by a penetrating wave. Hereby, the attenuation of the wave through the object is measured. This is done for various directions, penetrating the object on different paths. Afterwards, these measurements are used to estimate the attenuation coefficient of the considered object at every point.

It is very useful to organize the measurements by their angular direction in relation to the object. All measurements taken with the same angular direction form one projection of the measured object. In tomography a data set consists of projections for angles in a range from zero to 180 degrees. E.g. often equispaced angles $\alpha_k = \frac{k\pi}{n}$ for $k = 1 \dots n$, $n \in \mathbb{N}$ are used.

Limited angle tomography corresponds to the case where the angles of the projections are restricted by an interval. The acquisition angle of each measurement has to be within a given limited angular range, $\alpha_k \in [-\Phi, \Phi]$ for a given parameter value $\Phi \in [0, \pi]$. This parameter Φ is called the limiting or limited angle. Also in this case equispaced angles are common: $\alpha_k = -\Phi + k\frac{2\Phi}{n}$, $k = 1 \dots n$, $n \in \mathbb{N}$. In comparison to standard tomography the resulting data set is incomplete, as all angles outside the limited angular range $[-\Phi, \Phi]$ are missing.

We use a mathematical model to simulate the tomographic measurements. The Radon transform, introduced by Johan Radon in 1917 ([19]), describes the physical background of tomographic measurements. The projections are computed by integrals over oriented lines with specific angles and locations. We dedicate Section 1.1 to describe this mathematical model.

Afterwards we develop the reconstruction technique. We give an introduction to the curvelet transform and define it in continuous settings in Section 1.2. Curvelets were suggested to be used in reconstruction by E. Candès and D. Donoho in [3] and introduced in the field of limited angle tomography by J. Frikel in [13]. The connection between the measurements and the curvelet transform is given by the Projection Slice Theorem. Given the incomplete measurements in limited angle tomography, the Fourier coefficients of the considered object can be computed for certain angles in the Fourier space. The curvelet transform is defined in the Fourier space using a tiling that divides the plane into different angular areas. This can be used to concentrate on the areas that are given by the incomplete measurement data and exclude the areas that are not available from the reconstruction.

Another aspect is that curvelets form a tight frame of the vector space $L^2(\mathbb{R}^2)$ and are optimal for the sparse representation of objects with edges. Therefore they are suited for edge-preserving reconstruction.

Finally we are able to formulate the reconstruction problem using both, the Radon and the curvelet transform. We present an algorithm, the Iterated Soft-thresholding for sparse regularization in com-

bination with curvelets, introduced in [13]. We conclude this chapter by showing typical artifacts that occur in the reconstruction of tomographic data with a limited angular range.

1.1 Data Acquisition: The Radon Transform

In this section we follow the definitions given in [11] in order to introduce the Radon transform and the limited angle Radon transform. We will establish a connection between the Radon and the Fourier transform, which will become especially interesting, as soon as we consider the curvelet transform and its adaption to limited angle tomography in Chapter 2.

The Radon transform is commonly used to model the data acquisition process in x-ray tomography. One physical measurement uses a wave which is attenuated while penetrating the tissue along a line given by the location of the source of radiation and the receiver. This single measurement corresponds to the integration of the object along the given line. The Radon transform describes the measurements for a full scan of the object. I.e. the results of all lines penetrating the object are computed.

As a first step we define the oriented lines $l_{\theta,s} \coloneqq \{x \in \mathbb{R}^2 : \langle x, (\cos\theta, \sin\theta)^T \rangle = s\}$. A line $l_{\theta,s}$ has the normal direction $(\cos\theta, \sin\theta)^T$ and the distance from the origin $s \in \mathbb{R}$. Note, that this distance is directed and is allowed to be negative. This leads to the following identity:

$$l_{\theta,-s} = l_{\theta+\pi,s} \; \forall\, \theta \in [0, 2\pi],\; s \in \mathbb{R}. \tag{1.1}$$

For a better understanding, the definition of lines is depicted in Fig.1.1.

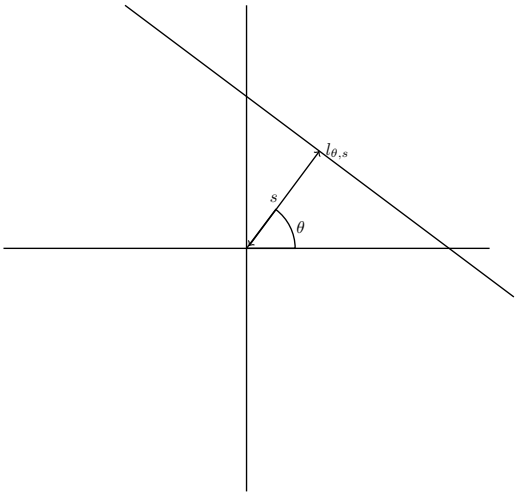

Figure 1.1: Parametrization of oriented lines in the plane.

Using this notation we are able to define the integral over an oriented line. In the following we assume f to be such that all stated integrals exist for all parameters (θ, s). We call this the natural

domain of the Radon transform.

$$\mathcal{R}f(\theta, s) = \int_{l_{\theta,s}} f(x)dS(x) = \int_{-\infty}^{\infty} f(s\cos\theta - x\sin\theta, s\sin\theta + x\cos\theta)dx. \tag{1.2}$$

The Radon transform $\mathcal{R}f$ is now defined as the collection of integrals of f along the lines in the plane. This defines a function on $\mathbb{R} \times [0, \pi]$.

In limited angle tomography the Radon transform is not available for the complete angular range, but only given for a limited angular range $\theta \in [-\Phi, \Phi]$. The angle $\Phi < \frac{\pi}{2}$ is called the limiting angle. We note this by $\mathcal{R}_\Phi f$ to emphasize that the Radon transform of f is defined only on the limited angular domain $[-\Phi, \Phi]\times\mathbb{R}$. The transform $\mathcal{R}_\Phi$ is called the limited angle Radon transform. The main problem with the limited angle Radon transform is that the corresponding reconstruction problem $y = \mathcal{R}_\Phi f$ is extremely ill-conditioned, as was shown in [8]. As a consequence small perturbations in the measurements can cause huge errors during the reconstruction process. In practice, this is especially troubling, since small corruptions of the measurements are always present as a consequence of noise.

1.1.1 Projection Slice Theorem

The Projection Slice Theorem, also called Fourier Slice Theorem, establishes a link between the Radon transform and the Fourier transform of a function.

Theorem 6.2.1 taken from [11]: Let f be an absolutely integrable function in the natural domain of the Radon transform $\mathcal{R}$. For any real number r and unit vector $\omega = (\cos\theta, \sin\theta)$, we have the identity

$$\int_{-\infty}^{\infty} \mathcal{R}f(s, \omega)e^{-isr}ds = \hat{f}(r\omega). \tag{1.3}$$

The proof of this theorem can be found, for instance, in [11] and is not given here.
The message of the theorem is: the results of the following two computations are the same for a two-dimensional function f:

a) compute the one-dimensional Fourier transform of a projection of f onto a line.

b) compute the two-dimensional Fourier transform and take the a slice of the Fourier plane parallel to the projection line in a) going through the origin.

For a better understanding, the Theorem is illustrated in Fig. 1.2.

The important consequence in limited angle tomography is that if the radon transform is available only for angles $\theta \in [-\Phi, \Phi]$, the Fourier plane of the measured function is given on two cones perpendicular to the measurement angles like illustrated in Fig. 1.3. This area in Fourier domain is called the visible cone and is defined properly at the beginning of Chapter 2. This separation of the Fourier space into angular segments, that are available and segments that are unavailable leads us to the curvelet transform.

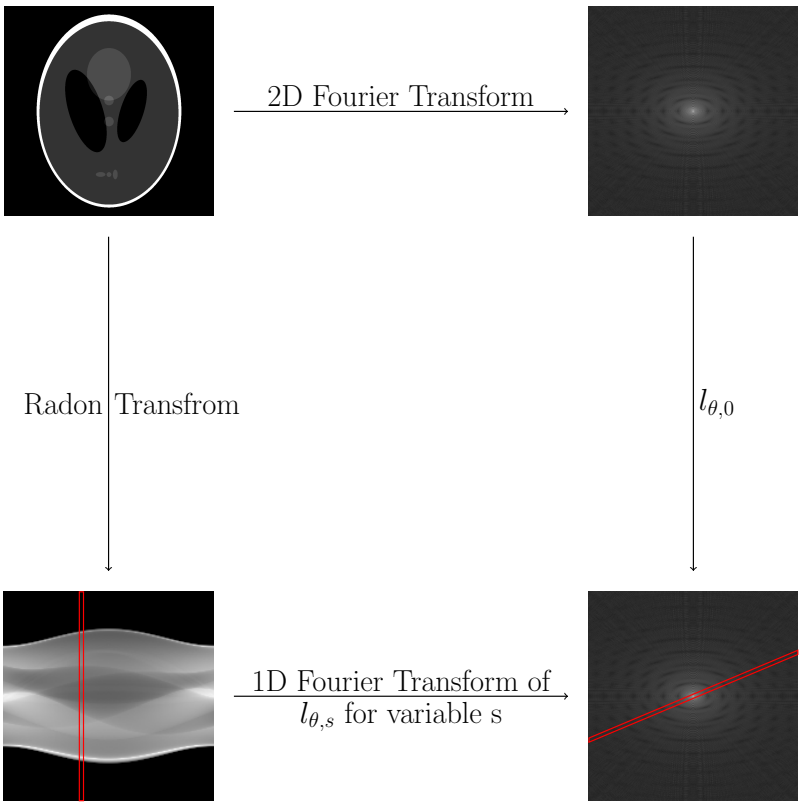

Figure 1.2: Illustrationof the Projection Slice Theorem

1.2 Curvelet Transform: Continuous Setting

The curvelet Transform is a multiscale, highly directional transform. Similar to the well known wavelet transform, or other (multiscale) transformations (Contourlet transform [9], Wedgelet transform [10], Bandlet transform [16]), the curvelet transform represents images or functions with the use of certain atoms, here called curvelets. Curvelets are essentially supported on an ellipse in spatial domain and supported on a polar wedge in frequency domain as can be seen for representative curvelets in Fig.(1.4). The last feature builds the connection to limited angle tomography. As in Fourier domain curvelets are supported on a polar wedge, we can distinguish curvelets that are defined in the measurable area from curvelets that lie in the not measurable area of the Fourier plane. This will become an important feature during reconstruction.

During this section we introduce the curvelet Transform, following the definitions given by Emanuel Candès et al. in [3] and [2].

1.2.1 Definition

Curvelets are defined in Fourier space. More precisely they are constructed by a tiling of the Fourier space. A sketch of it is shown in Fig. 1.5. The tiling is centered around the origin of the Fourier

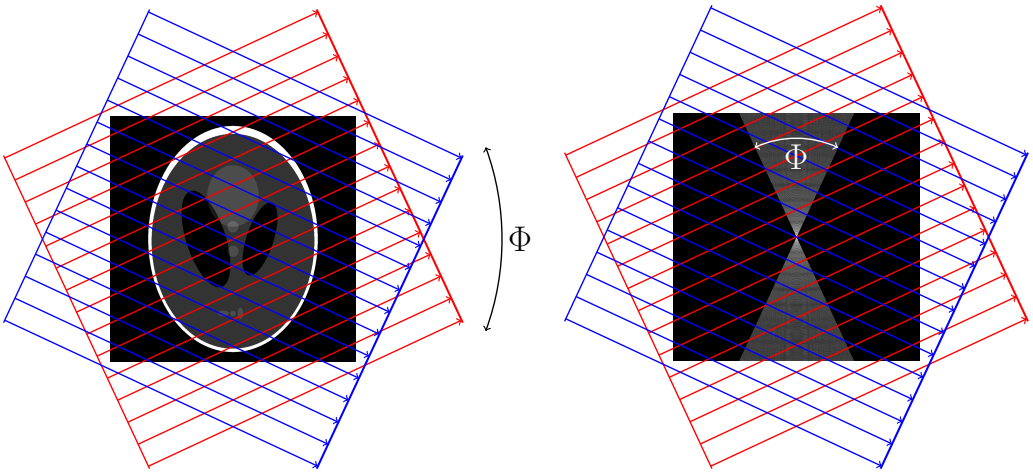

(a) Measurements in spatial domain (b) Computable coefficients in Fourier domain

Figure 1.3: Radon transform for a range of Φ angles and the corresponding Fourier plane given on the slices, perpendicular to the projection direction.

space and subdivides it into different radial scales. Points within a certain distance to the origin lie in the same radial scale. Additionally, each radial scale except the low pass element, the radial scale containing the origin, is subdivided into angular scales. Points within a certain angular range lie in the same angular scale. We firstly consider the fine scale elements, the element that do not contain the origin:

Here, the radial scale provides elements of different magnitude, whereas the angular scale determines the direction of an element. In addition to that, the location of a given element is influenced by a translation parameter $k \in \mathbb{N}^2$. Curvelets are defined via a generating curvelet $\Psi_{j,0,0}$ for each radial scale 2^{-j}, $j \in \mathbb{N}_0$ and a rotation according to an angular scale $l \in [1, 2, \ldots, 2 \cdot 2^{\lceil \frac{j+1}{2} \rceil - 1}]$. In order to define these generating curvelets, we introduce two window functions, $W(r)$ the "radial window" and $V(\omega)$ the "angular window", in the Fourier domain using polar coordinates (r, ω). Both windows are assumed to be smooth, non-negative and real-valued. Further,

$$\operatorname{supp} W \subset (1/2, 2), \ \operatorname{supp} V \subset [-1, 1] \tag{1.4}$$

and the admissibility conditions

$$\sum_{j=-\infty}^{\infty} W^2(2^j \cdot r) = 1, r \in (3/4, 3/2), \tag{1.5}$$

$$\sum_{l=-\infty}^{\infty} V^2(\omega - l) = 1, \omega \in (-1/2, 1/2), \tag{1.6}$$

are required to be satisfied.

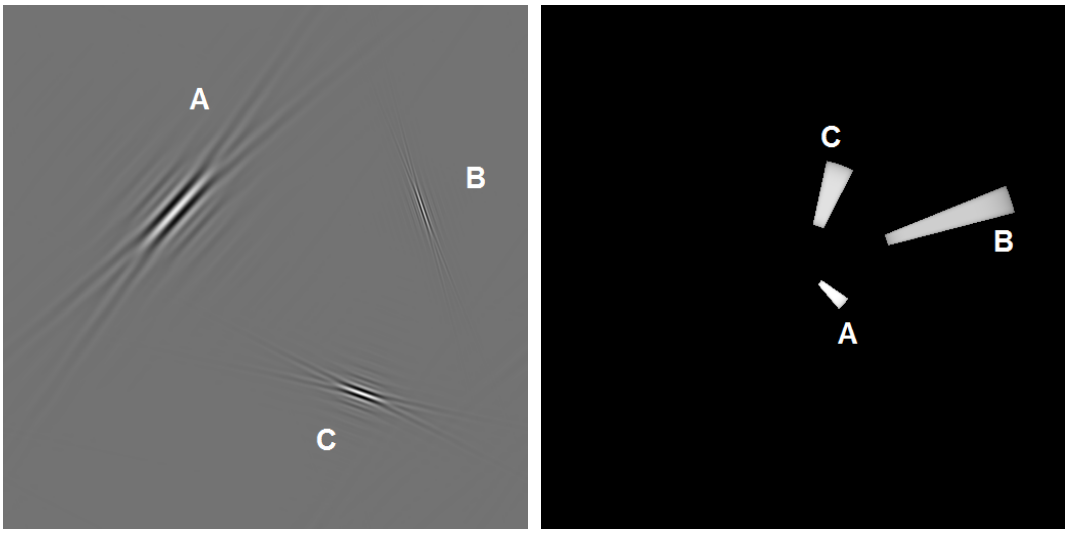

(a) Spatial domain (b) Fourier domain

Figure 1.4: Sum of three curvelet atoms at various scales, directions and translations in spatial domain and the modulus of it's Fourier transform in Fourier domain.

A generating curvelet $\Psi_{j,0,0}$ is defined in the Fourier domain using the product of the window functions W and V:

$$\hat{\Psi}_{j,0,0}(r,\omega) := 2^{\frac{-3j}{4}} \cdot W\left(2^{-j} \cdot r\right) \cdot V\left(\frac{2^{\lceil \frac{j}{2} \rceil + 1}}{\pi} \cdot \omega\right). \tag{1.7}$$

For $j \geq, l \in \{1, \ldots, 2^{\lceil \frac{j+1}{2} \rceil + 1}\}, k \in \mathbb{N}^2$ the curvelet $\Psi_{j,l,k}$ is defined by translation and rotation of its generating curvelet $\Psi_{j,0,0}$. Hence we introduce the (scale-dependent) equispaced sequence of rotation angles

$$\theta_{j,l} := l \cdot \pi \cdot 2^{-\lceil j/2 \rceil - 1}, l = 0, 1, \ldots, -2^{\lceil j/2 \rceil} \leq l < 2^{\lceil j/2 \rceil + 1}, \tag{1.8}$$

and the (scale-dependent) sequence of translation parameters

$$b_k^{j,l} := R_{\theta_{j,l}}^{-1}\left(\frac{k_1}{2^j}, \frac{k_2}{2^{j/2}}\right), k = (k_1, k_2) \in \mathbb{Z}^2, \tag{1.9}$$

where $R_\theta := \begin{pmatrix} \cos\theta & \sin\theta \\ -\sin\theta & \cos\theta \end{pmatrix}$ denotes the θ-rotation matrix and R_θ^{-1} its inverse.

Using these notations, we are able to define curvelets $\Psi_{j,l,k}(x), x \in \mathbb{R}^2$ at scale 2^{-j}, orientation $\theta_{j,l}$ and location $b_k^{j,l}$ by

$$\Psi_{j,l,k}(x) := \Psi_{j,0,0}(R_{\theta_{j,l}}(x - b_k^{j,l})). \tag{1.10}$$

Since $\operatorname{supp} W(2^j \cdot) \subset (1/2, \infty)$ for $j \in \mathbb{N}_0$, the region $\bigcup_{(j,l,k)} \operatorname{supp} \hat{\Psi}_{j,l,k}$ does not contain any low-pass elements. Therefore, similar to Wavelets, coarse scale elements have to be defined. This is accomplished by a low-pass function $\Psi_{-1,0}$ and its translates $\{\Psi_{-1,k}\}_{k \in \mathbb{Z}^2}$. As usual $\Psi_{-1,0}$ is given by

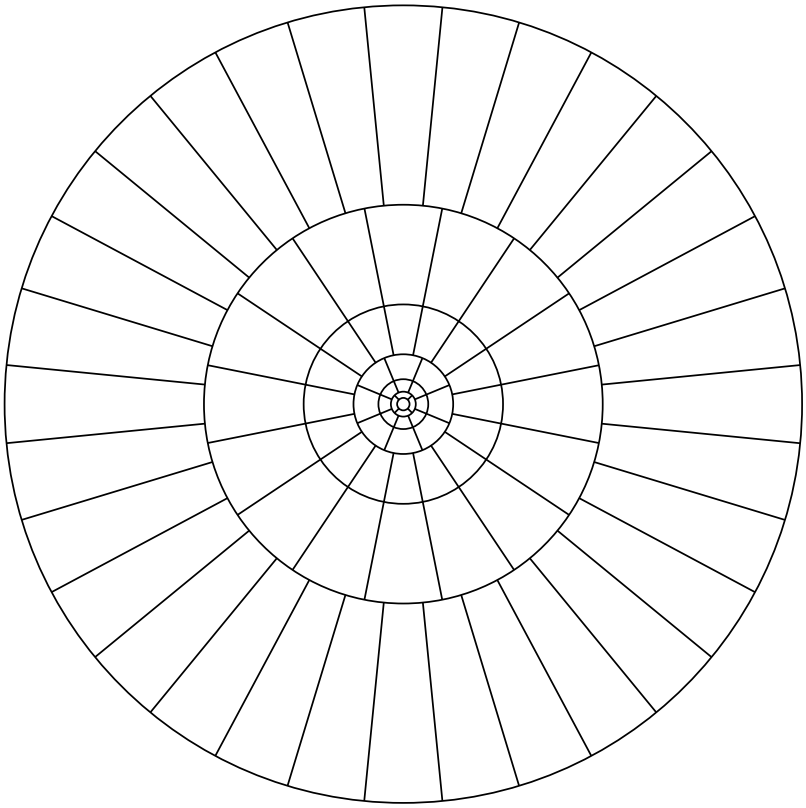

Figure 1.5: The standard tiling of the Fourier space used in the curvelet definition.

its Fourier transform:

$$\hat{\Psi}_{-1,0}(r,\omega) = W_0(r), \text{ with } W_0^2(r) := 1 - \sum_{j=0}^{\infty} W^2(2^{-j} \cdot r) \tag{1.11}$$

and $\Psi_{-1,k}$ derived by translation

$$\Psi_{-1,k}(x) = \Psi_{-1,0}(x - b_k^{-1,0}). \tag{1.12}$$

Note, that, as the low-pass curvelets $\Psi_{-1,k}$ are non-directional, no rotation of the generating curvelet is needed. Altogether the curvelet transform consists of two parts: The fine-scale, directional elements $(\Psi_{j,l,k})_{j>0,l,k}$ depicted in Fig.1.6(a) and the isotropic low-pass elements $(\Psi_{-1,k})_k$ depicted in Fig.1.6(b).

1.2.2 Features

Now that we have defined the curvelet system $\{\Psi_{j,l,k}\}_{j,l,k}$, we state some features that will be important for our work.

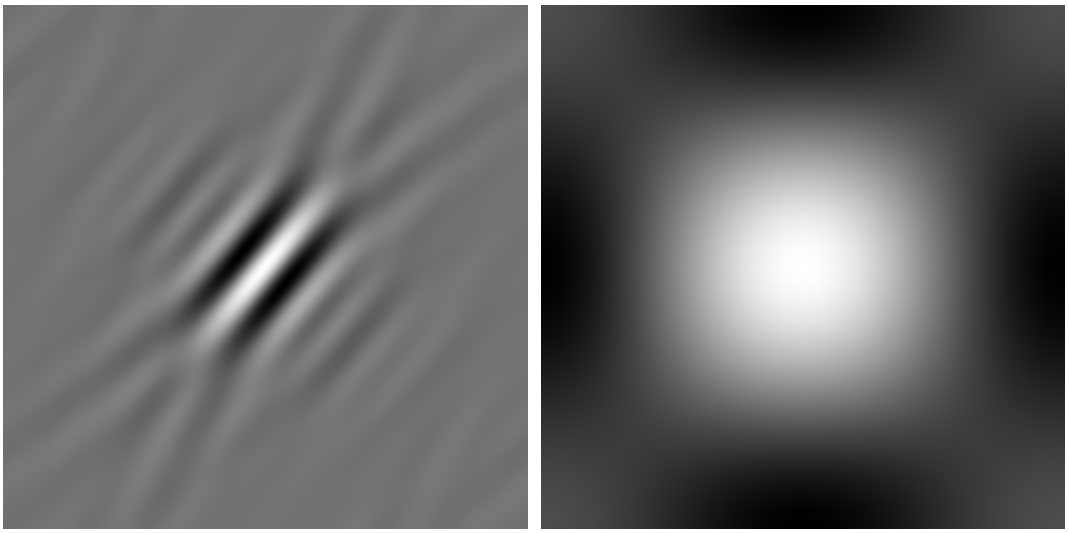

(a) Anisotropic fine-scale element (b) Isotropic low-pass element

Figure 1.6: Comparison of low-pass and fine-scale curvelet atoms in spatial domain.

Tight frame

One of the most important features of the curvelet transform is that the curvelet system constructed is a tight frame. A brief introduction to frames, a generalization of bases, where the uniqueness of representation is dropped and tight frames, frames with a minimal number of elements, is given in the Appendix. Similar to an orthonormal basis, we can represent a function $f \in L^2(\mathbb{R}^2)$ as a series of curvelets

$$f = \sum_{j,l,k} \langle f, \Psi_{j,l,k} \rangle \cdot \Psi_{j,l,k} \,. \tag{1.13}$$

Moreover, a Parseval relation holds true

$$\sum_{j,l,k} |\langle f, \Psi_{j,l,k} \rangle|^2 = \|f\|^2_{L^2(\mathbb{R})^2}, \; \forall f \in L^2(\mathbb{R})^2. \tag{1.14}$$

The term

$$c_{j,l,k}(f) \coloneqq \langle f, \Psi_{j,l,k} \rangle \tag{1.15}$$

is called curvelet coefficient of f for scale j, orientation or direction l and location k.

Sparse representation of Objects with C^2 Singularities

Curvelets yield an optimally sparse representation for functions that are C^2 except for discontinuities along C^2 curves [4].

This shows that curvelets are well suited to represent objects with edges. This feature is very important for using curvelets in the later reconstruction algorithm, as we aim on preserving edges.

In this context, sparse regularization and hence the sparse representation by curvelets is useful.

Tiling of the Fourier space

As stated before, every curvelet is compactly supported on a polar wedge in Fourier space. Hereby, all curvelets corresponding to the same scale and orientation parameters (j, l) belong to one single support wedge. The shape of the wedges obeys an anisotropic scaling relation "width $\approx$ length^2" with length $\approx 2^{-j}$ and width $\approx 2^{-2j}$ ([4]). This property is also called parabolic scaling ([2]).

There are $4 \cdot 2^{\lceil j/2 \rceil}$ angular wedges on each radial scale $j \in \mathbb{N}$. This means, starting with 4 wedges in the first and 8 in the second and third, the number of wedges doubles in every second scale. In opposition the length 2^j of the wedges doubles in every scale. This leads to a very characteristic tiling of the Fourier space by the wedges of all curvelets, as can be seen in Fig.1.5. (Note that the support of two adjacent wedges intersect. For simpler illustration this is not visible in Fig.1.5.)

Oscillatory behavior

In Fourier space a generating curvelet $\hat{\Psi}_{j,0,0}$ is supported away from the vertical axis, but near the horizontal axis. This results, in spatial domain, in a highly oscillatory behavior in horizontal direction and a low frequency in vertical direction. The same argumentation holds for any dilated and translated $\Psi_{j,l,k}$ leading, in spatial domain, to a low frequency in the perpendicular direction to the wedge orientation in Fourier space. This can be seen nicely in Fig.1.4. The essential support of a curvelet $\Psi_{j,l,k}$ is an ellipse located around $b_k^{j,l}$ in spatial domain.

1.2.3 Selection of the window functions

The window functions W and V form the core of the curvelet definition. Nevertheless, only two conditions have to be satisfied:

$$\operatorname{supp} W \subset (1/2, 2), \text{ and } \sum_{j=-\infty}^{\infty} W^2(2^j \cdot r) = 1, r \in (3/4, 3/2), \tag{1.16}$$

respectively

$$\operatorname{supp} V \subset [-1, 1], \text{ and } \sum_{l=-\infty}^{\infty} V^2(\omega - l) = 1, \omega \in (-1/2, 1/2). \tag{1.17}$$

In the following we present one possibility for the choice of these two functions taken from [17] and based on [6]. We consider the scaled Meyer windows

$$V(\omega) = \begin{cases} 1 & |\omega| \leq 1/3, \\ \cos\left(\frac{\pi}{2}\nu(3|\omega| - 1)\right) & 1/3 \leq |\omega| \leq 2/3, \\ 0 & \text{else}, \end{cases} \tag{1.18}$$

$$W(r) = \begin{cases} \cos\left(\frac{\pi}{2}\nu(5-6r)\right) & 2/3 \le r \le 5/6, \\ 1 & 5/6 \le r \le 4/3, \\ \cos\left(\frac{\pi}{2}\nu(3r-4)\right) & 4/3 \le r \le 5/3, \\ 0 & \text{else}, \end{cases} \tag{1.19}$$

where ν is assumed to be smooth and satisfies

$$\nu(x) = \begin{cases} 0 & x \le 0, \\ 1 & x \ge 1, \end{cases} \quad \nu(x) + \nu(1-x) = 1,\ x \in \mathbb{R}. \tag{1.20}$$

The function $\nu(x) = x$ for $x \in [0,1]$ satisfies Eq.(1.20) and leads to sufficient windows V and W. In order to receive smoother windows, ν has to be be chosen smoother. For example the polynomials $\nu(x) = 3x^2 - 2x^3$ or $\nu(x) = 5x^3 - 5x^4 + x^5$ for $x \in [0,1]$ lead to a higher order of smoothness. But also arbitrarily smooth functions are available:

$$\nu(x) = \frac{s(x-1)}{s(x-1) + s(x)},\ x \in [0,1], \tag{1.21}$$

with $s(x) = \exp\left(-\left(\frac{1}{(1+x)^2} + \frac{1}{(1-x)^2}\right)\right)$.

Using one of these choices, V and W satisfy the condition (1.16), respectively (1.17), and therefore are suitable for the use in defining curvelets. A plot of the window functions can be seen in Fig.1.7.

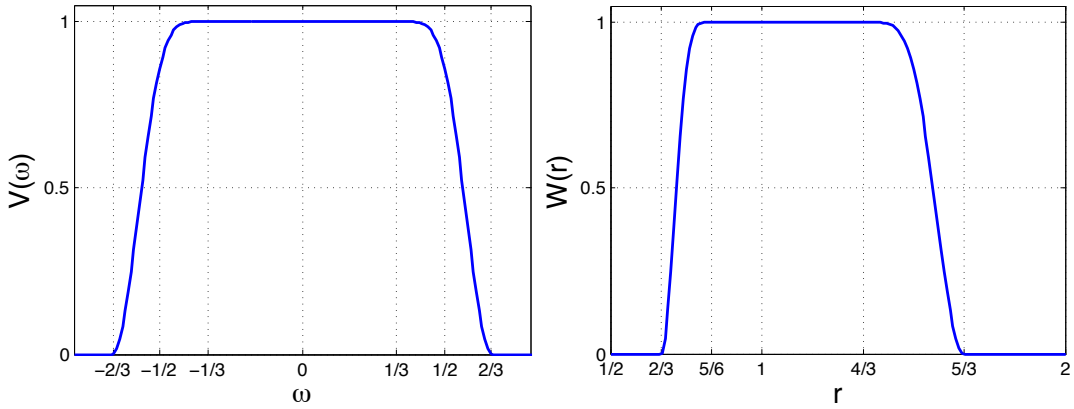

(a) Window function $V(\omega)$ (b) Window function $W(r)$

Figure 1.7: Plot of the scaled Meyer windows $V(\omega)$ and $W(r)$ using $\nu(x) = 5x^3 - 5x^4 + x^5$

1.3 Reconstruction via Curvelet Sparse Regularization

In this section we introduce the reconstruction method using the mathematical background we established in the last sections. Hereby, we follow the derivation of the so called Curvelet Sparse Regularization presented in [13].

The aim of the reconstruction procedure is to approximately compute the unknown function f from the measurements given by the data acquisition process. In our case this is the limited angle Radon transform $\mathcal{R}_\Phi f$. In a first step we will formulate the mathematical minimization problem using both, the Radon and the curvelet transform.

We have already mentioned in Section 1.1 that in practice the data acquisition is always corrupted by noise. Therefore the reconstruction problem is formulated as follows:

$$y^\delta = \mathcal{R}_\Phi f + \eta, \tag{1.22}$$

where η denotes the noise, $\delta > 0$ the noise level, i.e., $\|\eta\| < \delta$. Another consequence of the noise is, that the reconstruction has to be stable. At this point, we assume that the function f is C^2 except from discontinuities along C^2 curves. As discussed in Section 1.2 functions of this kind are optimally sparse with respect to the curvelet frame ([4]). Hence, the reconstruction process is stabilized by adding the constraint, that the solution of (1.22) has to be sparse with respect to the curvelet frame. We formulate the reconstruction problem in the curvelet domain to implement this. In other words we are no longer interested in recovering the function f directly, but in recovering the curvelet coefficients $c_{j,l,k} = \langle \Psi_{j,l,k}, f \rangle$ of f. Once we have the curvelet coefficients we are able to derive f by the use of the synthesis operator $f = T^* c = \sum_{i \in \mathcal{I}} c_i \Psi_i$. We reformulate the problem according to the curvelet coefficients:

$$y^\delta = \mathcal{R}_\Phi T^* c + \eta. \tag{1.23}$$

For simpler notation we define the operator $K :- \mathcal{R}_\Phi T^*$. Now, we can formulate the minimization problem by sparse regularization via the l^1-penalized Tikhonov type functional, i.e.,

$$\hat{c} = \underset{c \in \mathbb{R}^N}{\arg\min} \left\{ \frac{1}{2} \|Kc - y^\delta\|^2_{L^2(S^1 \times \mathbb{R}} + \|c\|_{1,w} \right\}, \tag{1.24}$$

where $\|c\|_{1,w} = \sum_k w_k |c_k|$ denotes the weighted 1-norm with a weight sequence w satisfying $w_k \geq w_0 > 0$.

In [7] it is shown that sparse regularization is indeed a regularization method. Therefore, the reconstruction process via (1.24) and $\hat{f} = \sum_{i \; in \mathcal{I}} \hat{c}_i \Psi_i$ is stable and favors sparse solutions [14]. This method is called Curvelet Sparse Regularization ([13]).

Now, that we have set up the minimization problem we concentrate on solving it. In the following we elaborate a minimization algorithm to find a minimum of Eq. (1.24). It was shown in [13] that the set of minimizers of the l^1-penalized Tikhonov functional

$$\Psi(c) = \frac{1}{2} \|Kc - y^\delta\|^2_{L^2(S^1 \times \mathbb{R})} + \|c\|_{1,w} \tag{1.25}$$

is non-empty and each minimizer $\hat{c}$ of Ψ is characterized by

$$\hat{c} = \mathcal{S}_{\gamma w}(\hat{c} - \gamma K^*(K\hat{c} - y^\delta)) \tag{1.26}$$

for any $\delta > 0$. The well known iterative soft-thresholding algorithm, introduced in [7] and [1], is used to minimize the problem (1.24). Modified to fit our situation, this algorithm consists of a fixed point iteration of Eq. (1.26):

$$\hat{c}^{n+1} = \mathcal{S}_{\tau^n}(\hat{c}^n - s_n K^*(K\hat{c}^n - y^\delta)). \tag{1.27}$$

This iteration can be divided into two consecutive parts: first a gradient descent step with step size s_n is performed. The step length s_n should satisfy

$$0 < \underline{s} \leq s_n \leq \bar{s} < \frac{2}{\|K\|^2}, \tag{1.28}$$

with $\underline{s}, \bar{s} > 0$ like described in [1]. Afterwards, soft-thresholding with respect to a thresholding sequence $\tau = (\tau_{(j,k,l)})_{((j,k,l)\in I)}$ is applied. In general, there is no rule how to choose this thresholding sequence. In [13] two different possibilities are discussed. The simplest way is a constant thresholding

$$\tau_{(j,l,k)} = \alpha, \tag{1.29}$$

for a suitable $\alpha > 0$. A second possibility is to adapt the thresholding sequence scale-dependently via setting

$$\tau_{(j,l,k)} = 2^{j-J}\sigma\sqrt{2\log_e N_{j,l}}, \tag{1.30}$$

where $N_{j,l}$ denotes the number of curvelet coefficients at scale 2^{-j} and at orientation $\theta_{j,l}$ and $J \in \mathbb{N}$ is the largest available scale parameter for the considered image. The parameter σ denotes the standard deviation of the noise η and can be estimated ([18, p. 565]), assuming additive white Gaussian noise, by

$$\sigma \approx 1.4826 MAD(c_J^n). \tag{1.31}$$

Here, $MAD(c_J^n)$ denotes the median of the absolute values of the curvelet coefficients c_J^n.

All in all we are now capable of solving problems in limited angle tomography. We have set up a minimization problem including a stabilization by sparse regularization. Furthermore, we stated a method to solve the given minimization problem using the iterative soft-thresholding algorithm. The algorithm is stated in Section 4.4, Algorithm 1.

1.4 Classification of Artifacts

This section is dedicated to the artifacts that are present in images from classical reconstruction methods in limited angle tomography. We use the Projection Slice Theorem presented in Section 1.1.1,

to calculate Fourier coefficients from the given measurements. Afterwards, this (incomplete) set of Fourier coefficients is transformed back using the inverse Fast Fourier Transform. This procedure is simple and fast, but, as we will see, causes strong artifacts in the resulting images. We show typical artifacts that can be found in the images and give some qualitative elements for their classification them. We give explanations of the source of these artifacts and how or whether one is able to reduce them. The possibility of reducing artifacts will be especially interesting in the later construction of an artifact-free reconstruction method.

We simulate the above described procedure by computing the Fast Fourier Transform of a given phantom, here the Shepp-Logan head phantom with improved contrast depicted in Fig. 1.8. After

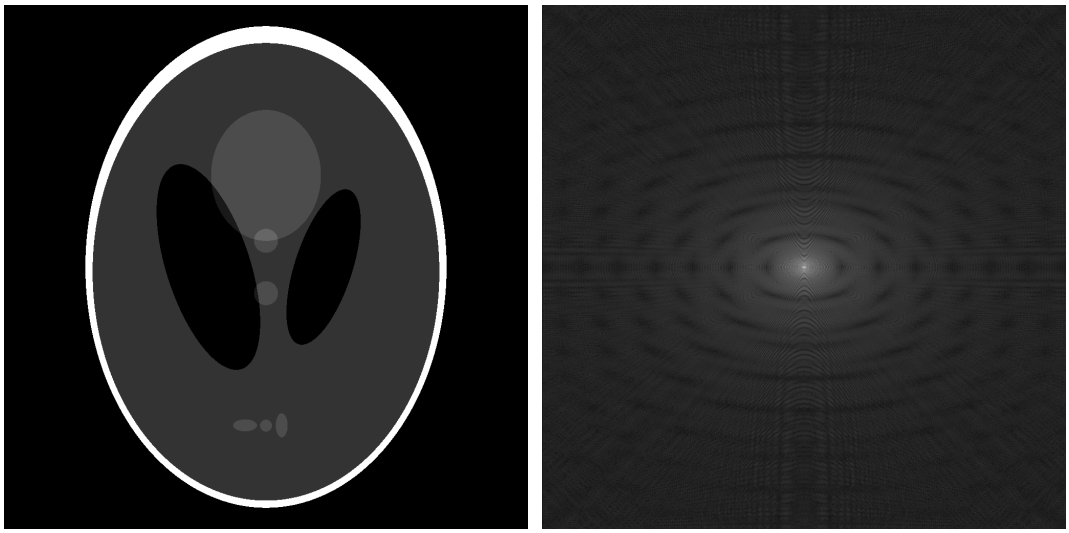

(a) In image domain. (b) In Fourier space

Figure 1.8: Shepp-Logan head phantom with improved contrast.

that, the Fourier plane is multiplied by a mask, setting all coefficients outside the computable angles of the Fourier plane to zero. The Fourier coefficients and the corresponding backtransformed images are shown in Fig.1.9. These images will be used to illustrate and classify artifacts in limited angle tomography. We make three observations:

- Due to the lack of Fourier coefficients not all edges of the original image can be found in the recovered image. This artifact is a direct result of the limited angle tomography itself and cannot be removed. Only singularities perpendicular to the given measurement directions are recoverable.

- The second apparent artifacts are the bright and dark lines covering the whole image. These artifacts are caused by the sharp cut off in the Fourier plane. These artifacts can be reduced or even removed. We will discuss this topic in greater detail after finishing the classification of the artifacts.

- A third class of artifacts can be seen solely at the location of the singularities of the original image. All along the original edges small point singularities are present. This is a result of the discretization process, causing curves to always have singularities in vertical and horizontal direction along each pixel. As horizontal singularities are recovered at this locations point singularities can be seen in the resulting image. We ignore these artifact, since they are only visible for the simulated measurements and will not be visible for real measurements.

In the following we concentrate on the bright and dark lines that are present in images from limited angle tomography. These lines are troublesome, as they reduce the image quality and can obscure structures in the image that can be important for the observer.

The source of these artifacts is the hard cut-off of the given coefficients in Fourier domain. This result can be showed by micro-local analysis [12, Chapter 3.4] using Wavefront sets [15, Chapter 8.1]. One possibility to prevent or reduce these artifacts is to avoid the hard cut-off. This can be achieved by smoothing the boundaries of the given cones in Fourier space. This fact, will be used in later chapters.

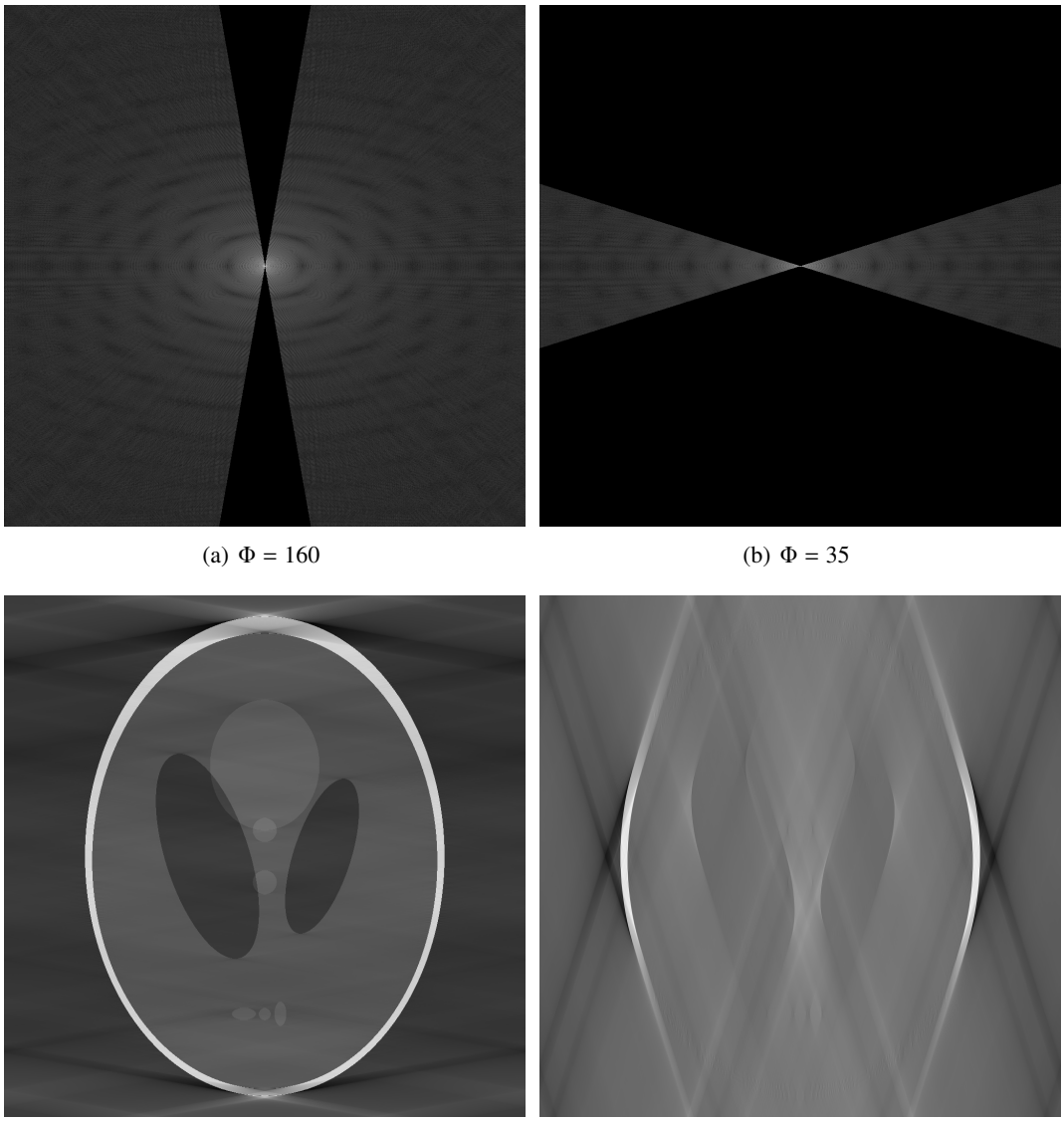

(a) Φ = 160 (b) Φ = 35

(c) Φ = 160 (d) Φ = 35

Figure 1.9: Images from limited angle tomography using reconstruction according to the Projection slice Theorem.

2 Adaption to limited angular range

In the present chapter we introduce an adaption of the curvelet Transform to the data acquired by limited angle tomography. This will be accomplished by different tilings of the Fourier space, covering not the whole angular range but concentrating on the angles for which measurements are available by the data acquisition process. This approach is motivated by the results presented in [13], especially Theorem 4.1:

Theorem 4.1 from [13]: Let $0 < \Phi < \pi/2$. We define the polar wedge W_Φ by

$$W_\Phi = \{\xi \in \mathbb{R}^2 : \xi = r(\cos\omega, \sin\omega), r \in \mathbb{R}, |\omega| \leq \Phi\}. \tag{2.1}$$

Moreover, we define the invisible subset of the curvelet index set by

$$\mathcal{I}_\Phi^{invisible} = \{(j,l,k) \in \mathcal{I} : \operatorname{supp} \hat{\Psi}_{j,l,k} \cap W_\Phi = \emptyset\}, \tag{2.2}$$

where $\Psi_{j,l,k}$ denotes a curvelet and $\mathcal{I}$ is the curvelet index set. Then,

$$\mathcal{R}_\Phi \Psi_{j,l,k} \equiv 0, \text{ for all } (j,l,k) \in \mathcal{I}_\Phi^{invisible}. \tag{2.3}$$

The message of this theorem is, that a curvelet whose support does not intersect with the polar wedge W_Φ in Fourier plane, lies in the kernel of the limited angle radon transform and therefore should not be considered in the reconstruction process. The proof of this theorem can be found in [13] and is not given here. In the following we refer to the polar wedge W_Φ as visible wedge or visible cone, since only points in Fourier space within this cone are visible to the data acquisition process.

Our adaption consists in two steps: first, all wedges of the tiling that are completely outside the visible cone are dropped. This step can be found in great detail in [13] and is described in Section 2.1. In a second step we do not only drop wedges, but also adjust the remaining wedges to fit the visible cone. This topic is discussed in Section 2.2.

2.1 Adaption by dimensionality Reduction

Theorem 4.1 motivates the following adaption to limited angle tomography, which can be found in greater detail in [13]. Here, the curvelet tiling itself stays untouched, only the wedges subtending the visible cone are considered, wedges without an intersection with the visible cone are neglected. To this end, the index set $\mathcal{I} = \mathcal{I}^{visible} \dot{\cup} \mathcal{I}^{invisible}$ is partitioned into the set of visible and invisible index

sets

$$\mathcal{I}_\Phi^{visible} = \{(j,l,k) \in \mathcal{I} : \operatorname{supp} \hat{\Psi}_{j,l,k} \cap W_\Phi \neq \emptyset\}, \tag{2.4}$$

$$\mathcal{I}_\Phi^{invisible} = \{(j,l,k) \in \mathcal{I} : \operatorname{supp} \hat{\Psi}_{j,l,k} \cap W_\Phi = \emptyset\}. \tag{2.5}$$

Coefficient for indices in the invisible set are excluded from the reconstruction process and are set

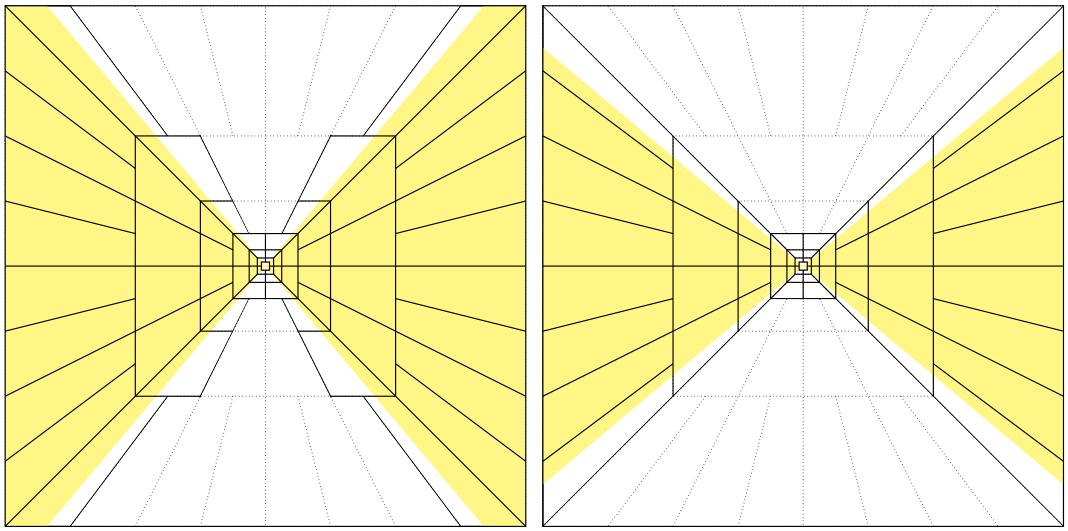

(a) $\Phi = 100°$ (b) $\Phi = 80°$

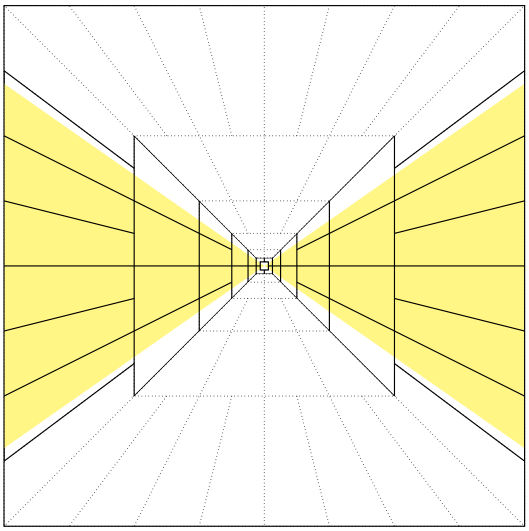

(c) $\Phi = 70°$

Figure 2.1: Adaption to limited angular range with standard tiling for various values of Φ. Corresponding visible cone shown in yellow.

to zero.

$$c_{j,k,l} := 0, \ \forall (j,k,l) \in \mathcal{I}_\Phi^{invisible} \tag{2.6}$$

This can be illustrated by removing the concerned curvelet wedges from the tiling. Some examples of resulting curvelet tilings are depicted in Fig. 2.1.

This procedure yields a significant dimensionality reduction of the reconstruction problem presented in Section 1.3. The problem can be reformulated in reduced form and reads

$$\hat{c}_\Phi = \underset{c\in\mathbb{R}^{N_\Phi}}{\arg\min}\left\{\frac{1}{2}\|K_\Phi c - y^\delta\|_2^2 + \|c\|_{1,w}\right\}, \tag{2.7}$$

where $N_\Phi = |\mathcal{I}^{visible}|$ and $(K_\Phi)_{m,n} = R_\Phi\Psi_n(\theta_m, s_m)$, $1 \le m \le M, n \in \mathcal{I}_\Phi^{visible}$ with parameters according to Section 1.3.

Depending on the angle Φ, the number of coefficients that have to be reconstructed is dramatically reduced. But the tiling does not necessarily fit to the visible cone, as can be seen in Fig.2.1. Depending on the limited angle the tiling still covers large areas outside the visible wedge. These points are still considered during reconstruction. Furthermore, the area outside the visible cone varies depending on the radial scale. The dimensionality reduction does not change the reconstruction problem. The solution of the reduced system is the same as the solution of the original one. This is a matter of fact, that only elements within the kernel of the limited angle radon transform, and hence the operator K_Φ, have been removed.

This leads us to a different, new approach by adjusting the curvelet tiling to a given visible wedge.

2.2 Further adaption by adjusting the curvelet tiling

In this section we no longer restrict ourselves to the standard tiling and the removal of invisible wedges. We adjust the tiling of the Fourier plane in order to match with the visible cone. In other words, we also change visible curvelet wedges in order to fit the visible cone. This changes the curvelet Transform and hence leads to a different reconstruction problem, as the operator K changes. In the following we present three approaches to adjust the tiling to the visible cone. We concentrate on three aspects of the tiling:

- The tiling, especially the boundaries, should be smooth, as we want to reduce artifacts.
- The tiling should be similar to the standard curvelet tiling, as we want to use the ideas and results from the standard curvelet transform.
- The tiling should allow as few points outside the visible wedge as possible, as we want to be optimally adapted to the visible wedge.

We present three different possibilities. These are based on the standard tiling for full angular range introduced in chapter 1.2, depicted in Fig.1.5 and can also be seen with consideration of the image boundaries in Fig.3.1.

For each of the following tilings we will outline the motivation and construction as well as some remarks.

2.2.1 Representation of one curvelet wedge in Fourier domain

At this point, we introduce the representation of a single wedge, in order to be able to understand the whole tiling in the later,. During this chapter a single wedge of the curvelet transform will be represented according to Fig.2.2 in Fourier domain. Hereby, the dashed area represents the part of

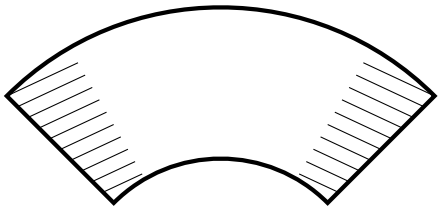

Figure 2.2: Representation of one curvelet in Fourier domain.

the wedge which is used for the fading in angular direction. More precisely, the area for which $V_{j,l,k}(\omega) \in (0,1)$, where $V_{j,l,k}$ denotes the angular window function corresponding to the curvelet $\Psi_{j,l,k}$. (Note, that only the fading in angular direction is depicted. The fading in radial direction is not shown, as we want to concentrate on the angular direction in this chapter. Therefore the wedge does not show the support of $\hat{\Psi}_{j,l,k}$, but only the area for which $(W_{j,l,k}(r))^2 \in (0.5,1)$, where $W_{j,l,k}$ denotes the radial window corresponding to $\Psi_{j,l,k}$. Nevertheless, the radial fading should be kept in mind.)

2.2.2 Inner Fading

The Inner Fading restricts the tiling to the visible cone. Only coefficients within the visible cone are allowed to be non-zero. Therefore the fading of the wedges at the angular boundaries closes with the visible cone. This prevents the reconstruction of coefficients, that were not measured during data acquisition. The smooth fading at the boundaries of the tiling is aimed at reduction of artifacts. The number of curvelet wedges is set to the number of wedges of the standard tiling within the visible wedge, in order to stay close to the standard curvelet transform.

Construction

Let the angle Φ be given. The number and location of the radial scales is taken from the standard tiling, defined in Section 1.2. We compute the number of wedges for each radial scale by taking $\frac{\Phi}{\pi}$ times the number of wedges of the standard tiling of that scale:

$$n_j = 2 \cdot \lceil \frac{\Phi}{2\pi} \cdot 2^{\lceil \frac{j+1}{2} \rceil} \rceil. \tag{2.8}$$

Now, we can calculate the wedge width *ww*, the width of the part of the wedge, where it is dominant, e.g. $V(\omega)^2 \in (0.5,1]$, and the wedge support width *wsw*, the width of the support of the wedge. At a first point in the construction of the tilings we have to decide which window functions are used.

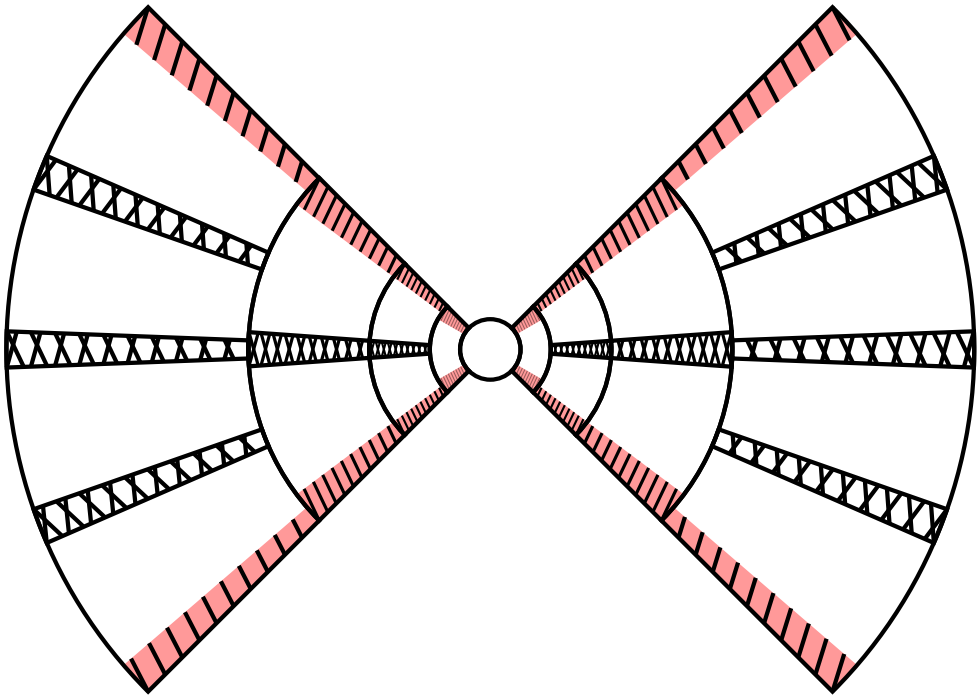

Figure 2.3: The Inner fading for $\Phi = 90°$.

We choose Meyer windows, like described in Section 1.2.3. The important feature is, that here at every end $\frac{1}{3}$ of the wedge width or equivalently $\frac{1}{4}$ of the wedge support width is used for the fading. This can be seen in Fig.2.4. For other window functions similar results can be derived and with this the following computation can be performed analogously. Solely the proportion of the fading area to the wedge width is of importance. In the case of Meyer windows, using the above mentioned proportions, we get

$$\Phi = n_j \cdot ww + \frac{1}{3}ww, \qquad \Phi = n_j \cdot wsw - (n_j - 1) \cdot \frac{1}{4}wsw. \tag{2.9}$$

and obtain

$$ww_j = \frac{\Phi}{n_j + \frac{1}{3}}, \qquad wsw_j = \frac{\Phi}{\frac{3}{4} \cdot n_j + \frac{1}{4}}. \tag{2.10}$$

Now we can compute the curvelet direction $\gamma_{j,k}$ in dependency of the radial and angular scale j, k

$$\gamma_{j,k} = \begin{cases} -\frac{\Phi}{2} + \frac{1}{6} \cdot ww_j + (k - 0.5) \cdot ww_j & 0 < k \leq \frac{n_j}{2}, \\ \text{for} & \\ \pi - \frac{\Phi}{2} + \frac{1}{6} \cdot ww_j + (k - 0.5) \cdot ww_j & \frac{n_j}{2} < k \leq n_j. \end{cases} \tag{2.11}$$

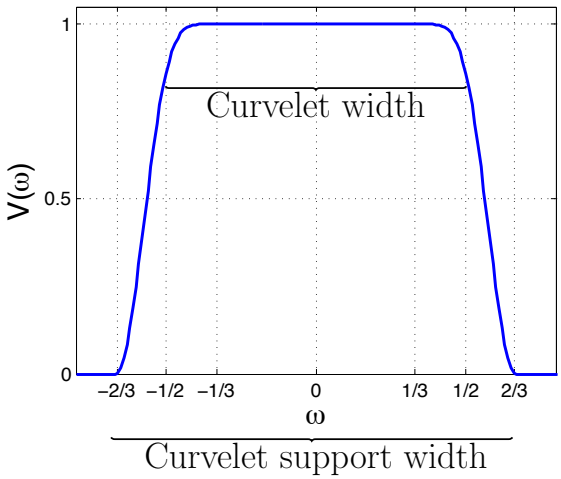

(a) Sketch of the angular window function $V(r)$

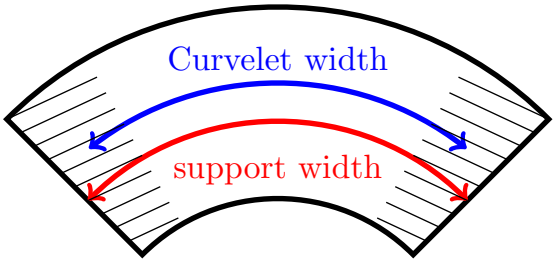

(b) Curvelet view

Figure 2.4: Sketch of curvelet width and support width.

Finally, we can evaluate the window functions and hence, compute the curvelet of radial and angular scale (j, k) in Fourier space, using polar coordinates

$$\hat{\Phi}_{j,k}(r, \omega) = V(2^{-j}r) \cdot W(|\omega - \gamma_{j,k}|). \tag{2.12}$$

Discussion

On one hand it is desirable to ignore all coefficients that are not measured during data acquisition and therefore lie outside the visible cone. On the other hand the problem is that we need smooth boundaries in order to reduce artifacts. This is due to the fact that a hard cutoff (at the border of the visible cone) leads to strong artifacts. Therefore, the only possibility to get a smooth cutoff is a lower weight of the values near to the angular boundaries, but within the visible wedge. Unfortunately, this fading inside the visible cone has consequences: The admissibility condition no longer holds true for every point within the visible cone. Hence, using this tiling, consecutive forward and backward curvelet transformations do not leave the image unchanged. For angles ω inside the region of the fading areas $W(\omega)^2 < 1$. Therefore consecutive forward and backward transformation smooth the Fourier cone of an image.

One further characteristic that occurs is the staircasing at the boundaries of the visible cone. As the number of angular wedges increases for higher radial scales, the fading area at the boundaries decreases. At this point it is important to recall, that there is a radial fading, too. This radial fading smoothes the staircases. Nevertheless, it is not apparent whether this has an influence on the resulting images, or not.

2.2.3 Outer Fading

The Outer Fading concentrates on improving two issues, that occurred, considering the Inner Fading. On the one hand side, every point inside the visible cone should be weighted in the same way. Hence, at every point inside the visible cone the squared weights should sum up to one. In other words: the admissibility conditions should be satisfied for each point inside the visible cone. On the other hand a hard cut-off at the boundaries of the visible wedge is not desirable in order to reduce artifacts. Therefore, values outside the visible cone have to be non-zero. These outside values are weighted the less the further away they are from the visible cone, decreasing smoothly to zero. The other issue with the Inner fading is that consecutive forward and backward transformations change an image. As a consequence of the alignment of the fading area with the visible wedge, here, the forward transform is inverted by a subsequent backward transform, if images are considered, that are supported inside the visible wedge in Fourier domain.

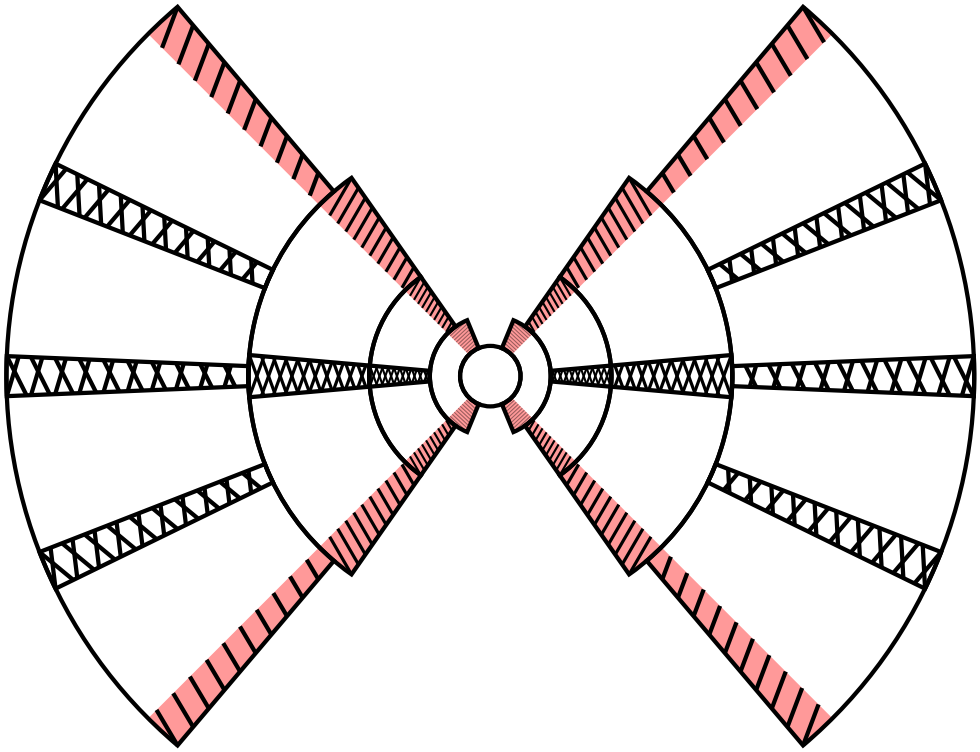

Figure 2.5: The Outer fading for $\Phi = 90°$.

Construction

Let the angle Φ be given. The number and location of the radial scales is taken from the standard tiling. Analogue to the construction of the Inner Fading we obtain the number of wedges for each

scale

$$n_j = 2 \cdot \left\lceil \frac{\Phi}{2\pi} \cdot 2^{\left\lceil \frac{j+1}{2} \right\rceil} \right\rceil. \tag{2.13}$$

Now we can calculate the wedge width *ww* and wedge support width *wsw*, defined in Section 2.2.2. Again, at this point we use the knowledge about the angular Meyer window function. The important feature is, that at each end $1/3$ of the wedge width is used for the fading. In case of another window function similar results can be computed. Analog to the Inner fading, we obtain

$$ww_j = \frac{\Phi}{n_j - \frac{1}{3}}, \qquad wsw_j = \frac{\Phi}{\frac{3}{4} \cdot n_j - \frac{1}{4}}, \tag{2.14}$$

using

$$\Phi = n_j \cdot ww - \frac{1}{3} ww, \qquad \Phi = n_j \cdot wsw - (n_j + 1) \cdot \frac{1}{4} wsw. \tag{2.15}$$

Note, that Eq.(2.10) for the Inner Fading and Eq.(2.14) here, only differ in the sign of the constants in the denominator.

Now we compute the curvelet direction γ in dependency of the radial and angular scale $\{j, k\}$

$$\gamma_{j,k} = \begin{cases} -\frac{\Phi}{2} - \frac{1}{6} \cdot ww_j + (k - 0.5) \cdot ww_j & k \leq \frac{n_j}{2}, \\ \text{for} & \\ \pi - \frac{\Phi}{2} - \frac{1}{6} \cdot ww_j + (k - 0.5) \cdot ww_j & k > \frac{n_j}{2}. \end{cases} \tag{2.16}$$

Finally, we can evaluate the window functions and hence, compute the curvelet of radial and angular scale (j, k) in Fourier space, using polar coordinates

$$\hat{\Phi}_{j,k}(r, \omega) = V(2^{-j} r) \cdot W(|\omega - \gamma_{j,k}|). \tag{2.17}$$

Discussion

In opposition to the Inner Fading, the weighting of the Outer Fading is very well motivated. For points inside the visible cone, the squared weight sums constantly up to one, leaving them untouched. But points outside the visible cone are constraint by a lower weight, depending on the angular distance to the visible cone. In order to reduce artifacts, this weighting decreases smoothly to zero. As a side effect of this, there are still parts of the tiling outside the window. This outside part of the tiling is minimal for the given number of angular scales.

Remarkable is, that the forward transform is inverted by the backward transform, as long as we consider images with corresponding Fourier transform supported inside the visible wedge. This is due to the fact that the admissibility conditions hold true for each point within the visible cone.

One characteristic that also occurs in the Outer fading is the staircasing at the boundaries of the visible cone. In opposition to the Inner Fading, here the staircases are located outside of the visible wedge, not inside. Like before, one has to keep in mind, that the staircases are smoothed due to

radial fading.

2.2.4 Uniform Fading

The Uniform Fading avoids the staircases at the boundaries of the visible wedge, which can be found in both, the Inner and Outer Fading. These are caused by the increasing number of angular wedges for higher radial scales. Therefore, we use the same, freely selectable angular range for the fading, independently of the radial scale. Hence, the same number of wedges is found in each radial scale. This tiling can be adapted to both, an Inner and an Outer Uniform Fading, where either the outer angle or the inner angle is aligned with the visible cone. This leads to either only coefficients within the visible wedge in case of the inner Uniform Fading or constant weight one within but also positive weights outside the visible wedge in case of the outer Uniform Fading.

Like before, this choice has consequences on the admissibility condition. For the Outer Uniform Fading this criterion is satisfied, as the squared weights sum up to one for each point inside the visible wedge. For the Inner Uniform Fading the admissibility condition does not hold true for each point inside the visible wedge.

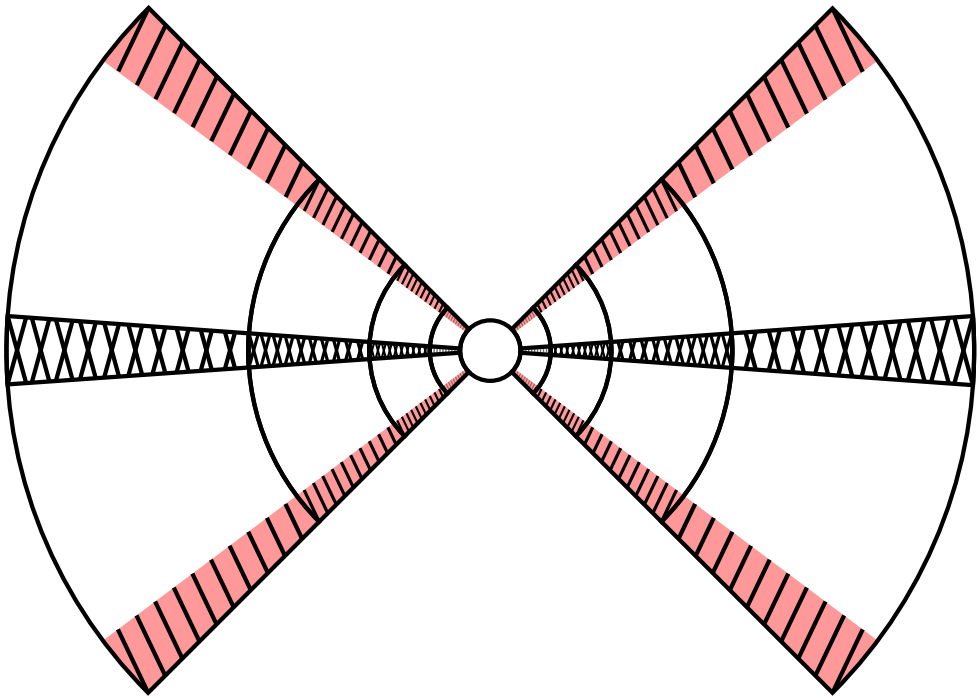

Figure 2.6: The Inner fading for $\varphi^i = 60°, \varphi^o = 90°$.

Construction

The uniform Fading requires three parameters. An inner angle $\varphi^i \in [0, \pi)$, an outer angle $\varphi^o \in (0, \pi]$ and the number $n \in \mathbb{N}$ of angular scales. But not every choice of parameters is possible. The fading

area has to be at most half of the curvelet wedge width. We have to check if a given parameter set is admissible, after the wedge width is computed.

If $Phi = \varphi^o$ and hence, the fading area lies inside the visible wedge, we denote the fading by Inner Uniform Fading, if $Phi = \varphi^i$ and hence, the fading area lies outside the visible wedge, we denote it by Outer Uniform Fading.

Like before, the number and location of the radial scales is taken from the standard tiling. The number of angular wedges is the same for every scale

$$n_j = n. \tag{2.18}$$

We can calculate the wedge width ww and wedge support width wsw, defined in the previous section, by considering

$$\frac{\varphi^o + \varphi^i}{2} = n \cdot ww, \qquad \varphi^o - \varphi^i = wsw - ww, \tag{2.19}$$

and obtain

$$ww = \frac{\varphi^o + \varphi^i}{2n}, \qquad wsw = \frac{\varphi^o + \varphi^i}{2n} + \varphi^o - \varphi^i. \tag{2.20}$$

As mentioned before, now we have to check if the parameters were chosen correctly. The fading areas starting at the opposing ends of the wedge must not overlap. To verify this, we compute the proportion f of the wedge width that is equal to one. This proportion has to be non-negative.

$$f = 1 - \frac{(\varphi^o - \varphi^i)}{ww} \overset{!}{\geq} 0. \tag{2.21}$$

As f varies depending on the parameters, we are no longer able to use the angular Meyer window function, since it has a fixed value of $f = \frac{2}{3}$. Therefore we will modify the function $V(\omega)$.

$$V_f(\omega) = \begin{cases} 1 & \omega \leq f, \\ \cos(\frac{1}{2-2\cdot f} \cdot (|\omega| - f) \cdot \frac{\pi}{2} & \text{for} \quad f < |\omega| \leq 2 - f, \\ 0 & \text{else.} \end{cases} \tag{2.22}$$

The function V_f is similar to the Meyer window function but modified with respect to the proportion f.

Now we are able to compute the curvelet direction γ in dependency of the angular scale k. Note that, as each radial scale has the same number of angular wedges, the curvelet direction depends

exclusively on the angular scale k and no longer on the radial scale j.

$$\gamma_k = \begin{cases} -\varphi^o + (k - 0.5) \cdot ww & k \leq \frac{n}{2}, \\ & \text{for} \\ -\varphi^o + (k - 0.5) \cdot ww + \pi & k > \frac{n}{2}. \end{cases} \tag{2.23}$$

Finally, we can evaluate the window functions and hence, compute the curvelet of radial and angular scale (j, k) in Fourier space, using polar coordinates

$$\hat{\Phi}_{j,k}(r, \omega) = V_f(2^{-j} r) \cdot W(|\omega - \gamma_k|). \tag{2.24}$$

Discussion

Depending on the choice of Inner or Outer Uniform Fading we find the same arguments like in the corresponding above cases. The curvelet transform with Inner Uniform Fading is not inverted by its backtransform, as the admissibility condition is not satisfied for each point within the visible cone. The Outer Uniform Fading solves this problem, but as a consequence of artifact reduction the tiling intersects with the invisible area of the Fourier space.

Additionally, the Uniform Fading causes more differences to the standard curvelet transform. The number of wedges of the Uniform Fading has no relation to the number of wedges in the standard tiling. Each angular wedge corresponds to a curvelet direction. A reduced number of wedges results in a lower sampling of the angles. This reduces number of modulations of a mother curvelet in the frame. This is compensated by a higher number of translates of a given modulation of a mother curvelet. Of course one can set the number of angular scales to the maximum of all radial scales of the standard tiling. Then it works the other way round. Lower scales are modulated more, but translated less. All in all, the Uniform Fading results in more differences to the original curvelet transform.

2.3 Conclusion

This chapter provides different possibilities to adapt the curvelet transform to a limited angular range during data acquisition. The basis for each approach is the fact, that wedges which do not subtend the visible cone lie in the kernel of the limited angle Radon transform. Therefore, as a first step, these invisible wedges are excluded from the reconstruction process. This leads to a significant dimensionality reduction of the reconstruction problem. Hereby, the degree of the dimensionality reduction depends on the limited angle Φ. The larger the limited angle, the higher is the dimension of the problem. More details on this approach can be found in [13].

We go further in the manipulation of the tiling. Not only do we drop wedges outside the visible cone, but we adapt the tiling itself to the given limited angle. This leads to three different strategies, depending on the weighting of the criteria we want to satisfy: on the one hand side we want to stay

close to the original curvelet tiling in order to use the results from the curvelet theory. Among others the sparse representation of objects with edges is important to us. On the other hand side, we want the tiling to cover as few points outside the visible cone as possible in order to prevent the reconstruction of points that were not measured. Another aspect we want to take care of is artifact reduction. This forces us to only consider smooth tilings. A hard cut-off at the boundary of the visible cone is not desirable, as this leads to strong artifacts.

For each of the three tilings presented, we give a brief motivation. We state on which aspects the single tilings concentrates: the Inner Fading completely excludes the invisible area of the Fourier plane. Unfortunately, combined with artifact reduction, this has unwanted consequences on the admissibility condition. The admissibility condition is no longer satisfied and hence, forward and backward transformations do no longer invert each other. To resolve this issue we introduce the Outer Fading. Here, the admissibility condition is satisfied. As a consequence of artifact reduction, however, some points outside the visible cone are considered and therefore reconstructed. In both, the Inner and Outer Fading staircasing at the boundary of the visible cone can be found. We present a third attempt, the Uniform Fading, which uses radial independent fading and therefore does not exhibit staircasing. This tiling can be used in an inner and outer variant. The drawback of this tiling is the fact, that it leads to more differences to the standard curvelet transform. For all possibilities we give the construction and some further remarks.

Each of the presented tilings is properly motivated and has its own focus. Therefore, at this point, it is not clear, which choice is to be preferred. We use all of the presented variants for numerical reconstruction and compare the results in chapter 4. There we line out the up- and downsides of the tilings.

But before we present the numerical results, we dedicate the following chapter to the construction of a fast discrete curvelet Transform.

3 Fast Discrete Curvelet Transform

In the present chapter we introduce a discrete version of the curvelet Transform discussed in Chapter 1.2. The implementation of the curvelet transform proposed by Candès et.al. in [2] uses the standard tiling shown in Fig.1.5 and is not optimized for the use in limited angle tomography. The implementation we develop in this chapter is independent of the tiling and can be used for the tilings introduced in Chapter 2. Therefore, our implementation is well suited for the use in limited angle tomography.

Firstly we present a minimal, straightforward workflow for the curvelet analysis and synthesis algorithms. This initial implementation of the transform exhibits some disadvantages. Among others we discuss unnecessarily slow computational time and an overcomplete representation of images in terms of an overcomplete sampling of curvelets in the image domain. We present a new approach to resolve the encountered drawbacks and obtain an advanced, fast curvelet transform with a minimal number of curvelet coefficients. These results are then presented, introducing the final analysis and synthesis algorithms which are suitable for tomographic reconstruction.

As a last point we conclude the chapter by comparing our implementation to the Fast Discrete Curvelet Transform proposed by Candès et.al. in [2].

3.1 Overcomplete Curvelet Transform

To begin with, we discuss a naive implementation of the curvelet analysis operator $\mathfrak{A} : \Omega \mapsto \mathbb{C}^p$, $\mathfrak{A}f = \{\langle f, \Psi_{j,l,k}\rangle\}_{j,l,k}$ described in Chapter 1.2. For a given image f, a set of coefficients $c_{j,k,l}$ is to be computed. The main result we use reads

$$c_{j,l,k}(f) = \langle f, \Psi_{j,l,k}\rangle = \int_\Omega \hat{f}(\xi)\hat{\Psi}_{j,l,k}(\xi)e^{i\langle b_k^{j,l},\xi\rangle}d\xi. \tag{3.1}$$

This representation of the coefficients leads us directly to the following straight forward approach:

3.1.1 Analysis Algorithm

We start with a given $n \times n$ image $f[n_1, n_2]$, $0 < n_1, n_2 < n$.

1. Firstly we compute the discrete 2D Fast Fourier Transform (FFT) $\hat{f}[n_1, n_2]$.
2. For each radial and angular scale $\{j, l\}$ we compute the curvelet $\hat{\Psi}_{j,l}[n_1, n_2]$ in the Fourier domain.

3. Now the point-wise products $\hat{\nu}_{j,l}[n_1, n_2] = \hat{f}[n_1, n_2] \cdot \hat{\Psi}_{j,l}$ are calculated.

4. The inverse discrete 2D Fast Fourier Transform (IFFT) yields the coefficient matrix $c_{j,l,k} = \nu_{j,l}[k_1, k_2]$.

The presented transform yields an $n \times n$ coefficient matrix $c_{j,l}$ for each scale pair $\{j, l\}$. This is due to the fact, that the radial and angular scale dependency in the translation factor was ignored by setting $b_k^{j,l} = R_{\Theta_{j,l}}^{-1}(k_1, k_2)$ and hence, every radial scale j is sampled in the same, overcomplete manner. This overcompleteness troubles in two aspects. It leads to more memory space, as more data is to be stored and slows down the computations with the coefficients during reconstruction steps.

3.1.2 Synthesis Algorithm

The synthesis operator $\mathfrak{S} : \mathbb{C}^p \mapsto \Omega$, $\mathfrak{S}\{c_i\}_i = \sum_{i=1}^{p} c_i \Psi_i$ is the adjoint to the analysis operator $\mathfrak{A}$. For a given set of coefficients $c_{j,l,k}$ the represented image f is to be computed. In the present case it consists simply in executing the inverse of each step in the appropriate order:

4'. The discrete 2D-FFT of each coefficient matrix is computed: $\nu_{j,l}[k_1, k_2] = \mathrm{FFT}(c_{j,l})$.

2'. For each radial and angular scale $\{j, l\}$ we compute the curvelet $\hat{\Psi}_{j,l}[n_1, n_2]$ in the Fourier domain.

3'. Now the point-wise product $\hat{\kappa}_{j,l}[n_1, n_2] = \hat{\nu}_{j,l}[n_1, n_2] \cdot \hat{\Psi}_{j,l}$ is calculated.

1'. At last we compute $f[n_1, n_2] = IFFT(\sum_{j,l} \hat{\kappa}_{j,l}[n_1, n_2])$ the 2D-IFFT of the sum of the product.

The Synthesis Operator can be seen as the inversion of the analysis Operator. consecutive executions of the synthesis algorithm after the analysis algorithm yields the input $f[n_1, n_2]$. (At least if minor errors due to machine precision are neglected.) Two facts are to be remarked here: Firstly each step in the analysis algorithm is inverted and executed in opposite order except for step 3. This step is the same for both, the analysis and the synthesis. But as long as the admissibility condition

$$\sum_{j=-\infty}^{\infty} |\hat{\Psi}(2^{-j}\xi)|^2 = 1, \; \xi \in \mathbb{R} \tag{3.2}$$

is satisfied, this yields the desired output. Equation 3.2 is a direct consequence of the admissibility conditions 1.5 and 1.6.

3.1.3 Discussion

The operators presented in Sections 3.1.1 and 3.1.2 are very simple to implement. Unfortunately, they exhibit some major drawbacks. This transform is very inefficient in two ways:

1. In step [2.] and [2'.] the curvelets are computed for every point (n_1, n_2). This computation is very time-consuming and, as a lot of curvelets have to be computed, it slows down both, the analysis and the synthesis, significantly. Moreover it is also unnecessary, as curvelets are supported on a polar wedge and as a matter of fact only a small fraction has to be computed. We dedicate section 3.2 to the solution of this rather technical problem.

2. The second problem concerns the output of Algorithm 3.1.1. The scale dependent translation is ignored and therefore a complete sampling in every scale is obtained. This corresponds to an overcomplete representation with a highly redundant frame set $\{\Psi_{j,k,l}\}$. As a result, more memory space is needed and the computation is decelerated in the analysis and synthesis algorithms. This is especially bothering during the tomographic reconstruction, as here calculations with the unnecessary large number of coefficients have to be made. Section 3.3 is dedicated to the solution of this problem.

Note, that the first drawback can be resolved without changing the transform. Drawback 2. on the other side is a far-reaching problem. Therefore the solution of this problem will be more ambitious and will need some structural changes of the algorithms. Nevertheless we start by solving the first drawback.

3.2 Fast curvelet computation

One of the most time-consuming parts of the digital curvelet transform is the computation of the single curvelets. This is aggravated by the fast growing number of curvelets in higher radial scales and the fact, that each curvelet is of the size of the original image. In the case of a full angular range, for an 128×128 image 113 curvelets, each again with 128×128 pixels, have to be computed; a 256×256 image yields 177 curvelets of size 256×256 and a 512×512 image yields 241 curvelets of size 512×512. It is apparent, that the computation of a single curvelet should be optimized as much as possible in order to keep the computational time at a minimum.

For every curvelet in Fourier space the product of the window functions W and V has to be evaluated for every pixel of the $n \times n$ image. Recalling the definition of a single curvelet, we notice, that the product is supported on a polar wedge. In other words: We know that outside this wedge the curvelet is zero. Now, we use this fact in order to compute only the non-zero values and set the others to zero by default. (Or even better: We memorize which values we have computed and save memory space by not storing the zero values.) The simplest (and in MATLAB possibly the most efficient) way is to compute the smallest axial-aligned rectangle containing the complete support of the considered curvelet. Then the data points within this rectangle are computed as usual, by (matrix-valued) evaluation of the window-functions $W(r)$ and $V(\omega)$, but the entries outside the rectangle are set to zero. This procedure leads to a major speed-up, as the ratio of the rectangle to the whole matrix is very low, as can be seen in Fig.3.1.

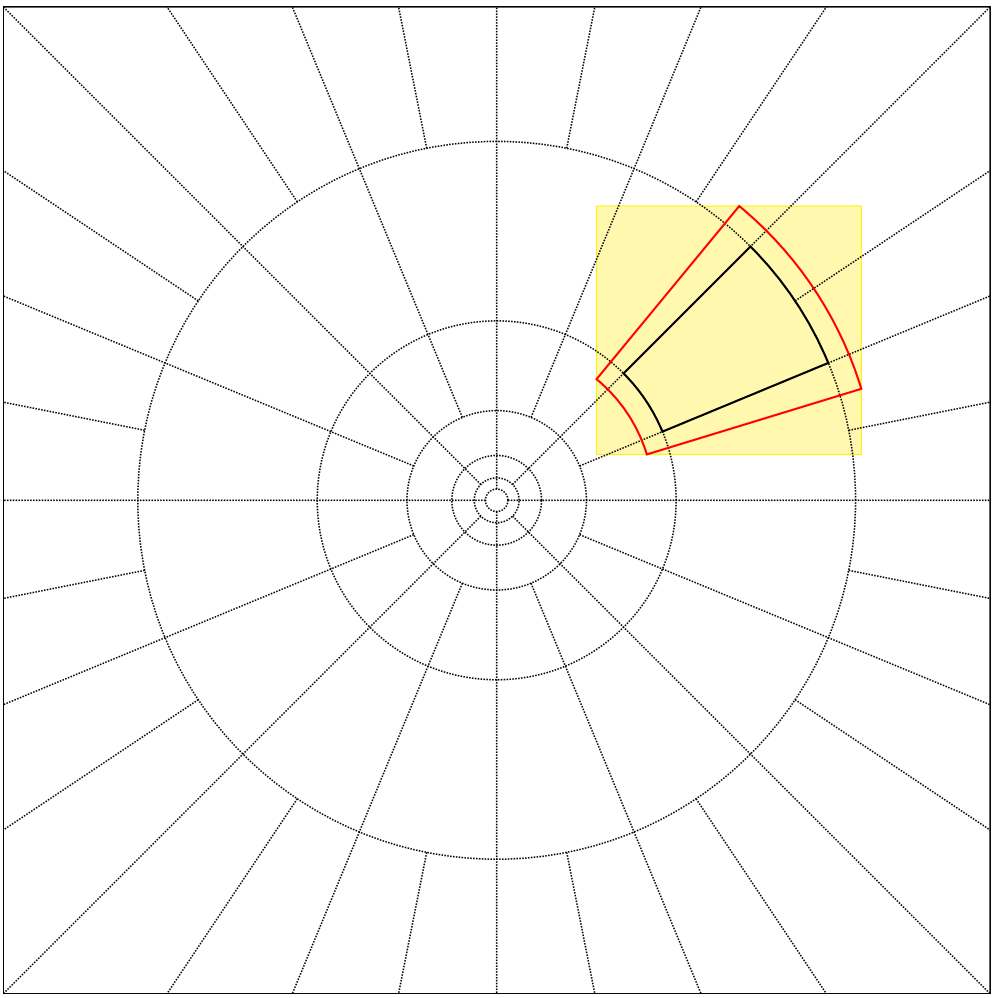

Figure 3.1: Comparison between the whole image and the area that actually has to be computed (shown in yellow) for one representative curvelet. Support of the considered curvelet shown in red.

In order to compute the described rectangle, we have to know the coordinates of the four edges of the curvelet wedge. Lets firstly rethink what kind of information is available to compute a curvelet and how we can use it to calculate the needed points. To begin with, we have the radial and angular index of the considered curvelet. The radial index yields the minimal radius r_{min} and maximal radius r_{max} of the wedge, meaning the minimal resp. maximal distance of the wedge to the origin. From the angular index we can derive the curvelet direction α, the curvelet width γ, the width of the part of the wedge, where it is dominant, e.g. $V(\omega)^2 \in (0.5, 1]$ and finally the curvelet support width σ, the width of the support of the wedge. Using these information we are able to calculate the lower left and upper right point of the rectangle. In the following we present this computation in greater detail.

3.2.1 Computation of the radii

In order to compute r_{min} and r_{max}, the minimal and maximal distance of the wedge to the origin, we revise one property from the definition of the radial Window $W(r)$:

$$\operatorname{supp} W \subset (1/2, 2), \tag{1.4a}$$

and one from the scaling of a single curvelet:

$$\hat{\Psi}_{j,0,0}(r,\omega) := 2^{\frac{-3j}{4}} \cdot W\left(2^{-j} \cdot r\right) \cdot V\left(\frac{2^{\lceil \frac{j}{2} \rceil - 1}}{\pi} \cdot \omega\right). \tag{1.7}$$

From the scaling $\left(2^{-j} \cdot r\right)$ of the radial window function one can see, that the radial value 2^j in Fourier domain corresponds to 1 in the radial-window domain and 2^{j+1} corresponds to 2. Therefore, considering Eq.(1.4a), the radial support of the wedge lies in $(2^{j-1}, 2^{j+1})$ as $W(r) = 0$ for $r < 0.5 = 2^{-j} * 2^{j-1}$ and $r > 2 = 2^{-j} * 2^{j+1}$. This yields $r_{min} = 2^{j-1}$, $r_{max} = 2^{j+1}$.

These borders are the minimal and maximal borders for any choice of the window function $W(r)$. For a specific choice we can get an even larger minimal and lower maximal border. E.g. the Meyer windows introduced in Section 1.2.3 are supported in $(2/3, 5/3) \subsetneq (1/2, 2)$. This choice leads to the following borders,

$$r_{min} = 2^j - \frac{2}{6}2^j = \frac{2^{j+1}}{3}\,, \tag{3.3}$$

$$r_{max} = 2^{j+1} - \frac{2}{6}2^j = \frac{5}{3}2^j\,, \tag{3.4}$$

as can easily be derived by considering Fig.3.2: like before $W(1)$ corresponds to 2^j and $W(2)$ to 2^{j+1}. Therefore one unit in the window-function domain corresponds to 2^j units in the Fourier domain. We have to subtract $2/6$ units from 1 to get to the minimal non-zero value, hence, yielding Eq.(3.3). With the same argumentation we reach the maximal non-zero value by subtraction $2/6$ units from 2, resulting in Eq.(3.4).

3.2.2 Computation of the angles

Similar to the computation of the radii we need to revise two properties from the definition of the (in this case angular) window and the scaling in the definition of the mother curvelet:

$$\operatorname{supp} V \subset [-1, 1], \tag{1.4b}$$

$$\hat{\Psi}_{j,0,0}(r,\omega) := 2^{\frac{-3j}{4}} \cdot W\left(2^{-j} \cdot r\right) \cdot V\left(\frac{2^{\lceil \frac{j}{2} \rceil + 1}}{\pi} \cdot \omega\right), \tag{1.7}$$

As we already know from the tiling of the Fourier space in section 1.2.2, the standard tiling is subdivided into $2^{\lceil j/2 \rceil + 2}$ angular wedges for a radial scale j. Using this, we can derive the curvelet

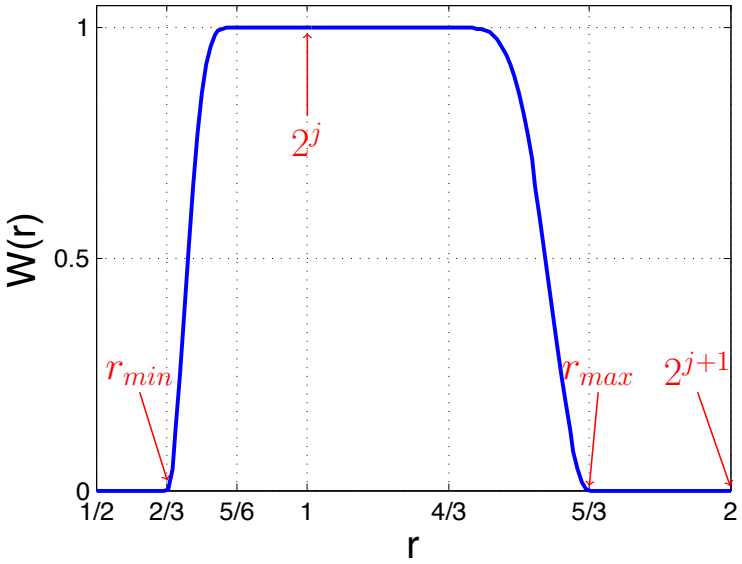

Figure 3.2: Sketch of the radial window function $W(r)$

width γ, the width, where the curvelet is dominant, e.g. the value is larger than 0.5:

$$\gamma = \frac{2\pi}{2^{\lceil j/2 \rceil + 2}} = \frac{\pi}{2^{\lceil j/2 \rceil + 1}} \tag{3.5}$$

With this $\gamma/2$ in Fourier domain corresponds to $\frac{2^{\lceil \frac{j}{2} \rceil + 1}}{\pi} \cdot \frac{\gamma}{2} = \frac{1}{2}$ in angular window domain. Hence, using Eq.(1.4b) the curvelet support width σ is maximal 2γ.

Again, this is the maximal support width for any choice of $V(\omega)$. For a specific choice we can get a smaller support width. In the case of Meyer windows V is supported in $[-2/3, 2/3] \subsetneq [-1, 1]$ and leads to curvelet support width $\sigma = \frac{4}{3}\gamma$ as depicted in Fig.3.3.

for the adapted tilings presented in Chapter 2, the curvelet width and support width is given in the construction sections.

3.2.3 Computation of the smallest axial aligned rectangle

With the computed values r_{min}, r_{max} and σ we can now derive the coordinates of the edges of the wedge, labeled in Fig.3.4. As we know the distance to the origin and the angles the points lie on, the

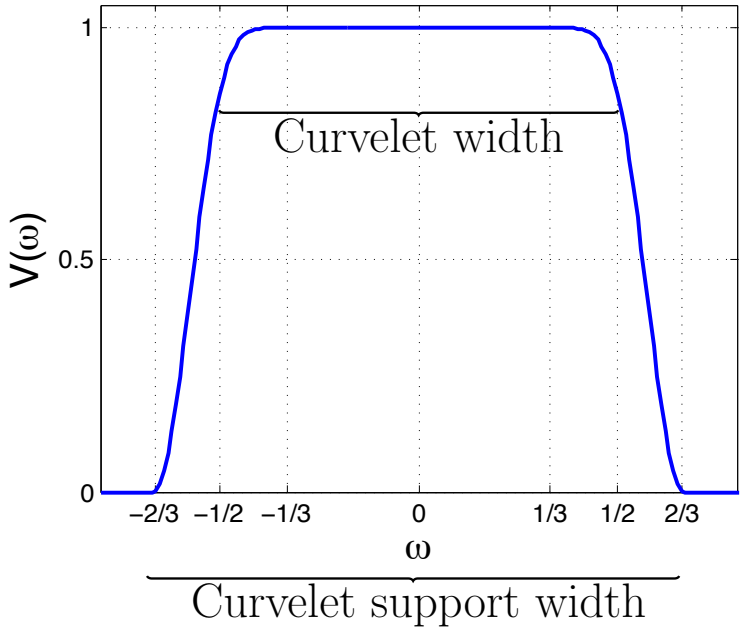

Figure 3.3: Sketch of the angular window function $V(r)$

coordinates can be calculated by transformation from polar to Cartesian coordinates. We obtain

$$\begin{aligned} tl &= r_{max} \cdot (\sin(\alpha + \frac{1}{2}\sigma), \cos(\alpha + \frac{1}{2}\sigma)), \\ tr &= r_{max} \cdot (\sin(\alpha - \frac{1}{2}\sigma), \cos(\alpha - \frac{1}{2}\sigma)), \\ bl &= r_{min} \cdot (\sin(\alpha + \frac{1}{2}\sigma), \cos(\alpha + \frac{1}{2}\sigma)), \\ br &= r_{min} \cdot (\sin(\alpha - \frac{1}{2}\sigma), \cos(\alpha - \frac{1}{2}\sigma)). \end{aligned} \tag{3.6}$$

Using these points, we can easily compute the coordinates of the points rl and rt, representing the rectangle R. The point rl consist of the minimal x and y values of Eq.(3.6), the point rt consists analogously of the maximal x and y values of Eq.(3.6). Additionally one special case has to be considered. If the horizontal axis lies inside the angular support, the point $(r_{max}, 0)$ has to be added to the maximization process.

These argumentations only fit if the curvelet direction lies in the East region of the image, e.g. $\alpha \in [-\pi/4, \pi/4]$. The other three cases follow analog.

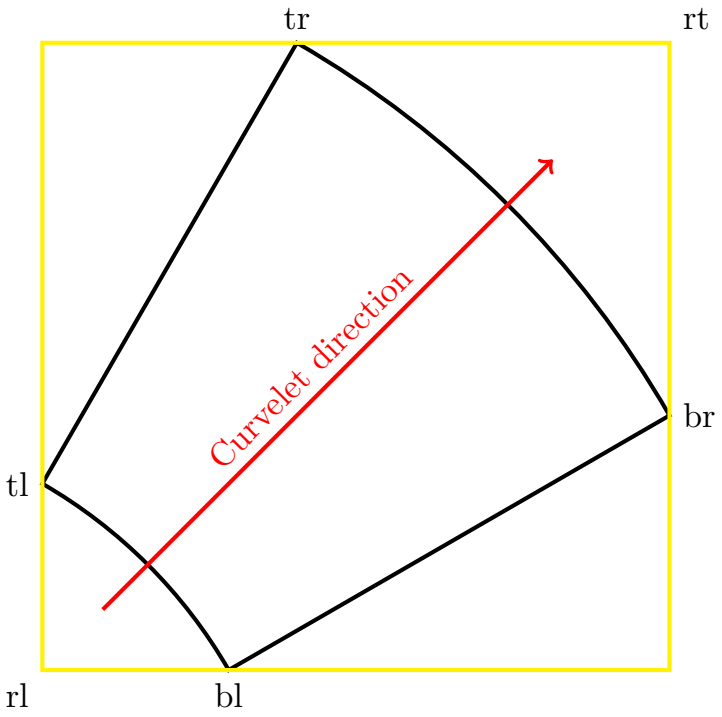

Figure 3.4: Sketch of one curvelet with curvelet direction α and curvelet support width σ

3.3 Reduction of Curvelet Coefficients: From overcomplete to tight Frames

As mentioned in Subsection 3.1.3, the analysis algorithm introduced in the beginning of this chapter computes an overcomplete set of coefficients. This means, that the curvelet dictionary $\{\Psi_{j,l,k}\}$, used to represent a given image f, contains more elements than needed. In other words, the same image can be represented by a smaller dictionary and hence, less coefficients. Besides this mathematically nicer representation, it also has a practical advantage, as it results in a lower memory space requirement. This is especially noticeable during the reconstruction, when calculations with and modifications of the coefficients have to be made.

Using the naive implementation, presented at the beginning of this chapter, for each pair $\{j,l\}$ of radial and angular scale an $n \times n$ coefficient matrix is generated. Hereby each coefficient $c_{j,l,k}$ corresponds to the curvelet $\Psi_{j,l,k}$ in image domain. Our goal is to represent the product $(\hat{f} \cdot \hat{\Psi}_{j,l,\cdot})[n_1, n_2]$ by a matrix $c_{j,l}$ of smaller size without loosing any information.

Once again we can use the fact, that each curvelet is supported on a polar wedge in Fourier space. A first attempt to reduce the number of coefficients is to compute the smallest rectangle R containing the support of a given curvelet like described in Section 3.2 for a fast curvelet computation. Instead of the whole image only the rectangle R is back-transformed using the inverse fast Fourier transform. This method can be nicely interpreted, as it corresponds to a translation of the rectangle to the center

of the Fourier plane. Hence, it corresponds to a modulation in the curvelet coefficient domain. Therefore, the smaller coefficient matrix corresponds to a downsampled version of the originally overcomplete coefficient matrix. In other words only every m-th coefficient in the bigger matrix is allowed to be non-zero, where m is the proportion of the size of R to the whole image size. It is easy to see, that the corresponding, smaller set of curvelet atoms is still a frame, as no information was lost.

But does this go far enough or is there a way to get even less coefficients without information loss? One conspicuity is, that the number of coefficients varies depending on the direction of the considered curvelet. The reason for this is, that, like depicted in Fig.3.5, the size of the rectangle R changes as soon as the curvelet direction is changed. This change in the sampling frequency seems rather unmotivated and we will see, that it leads to an unnecessarily larger coefficient matrix, if the curvelet direction is not horizontal nor vertical.

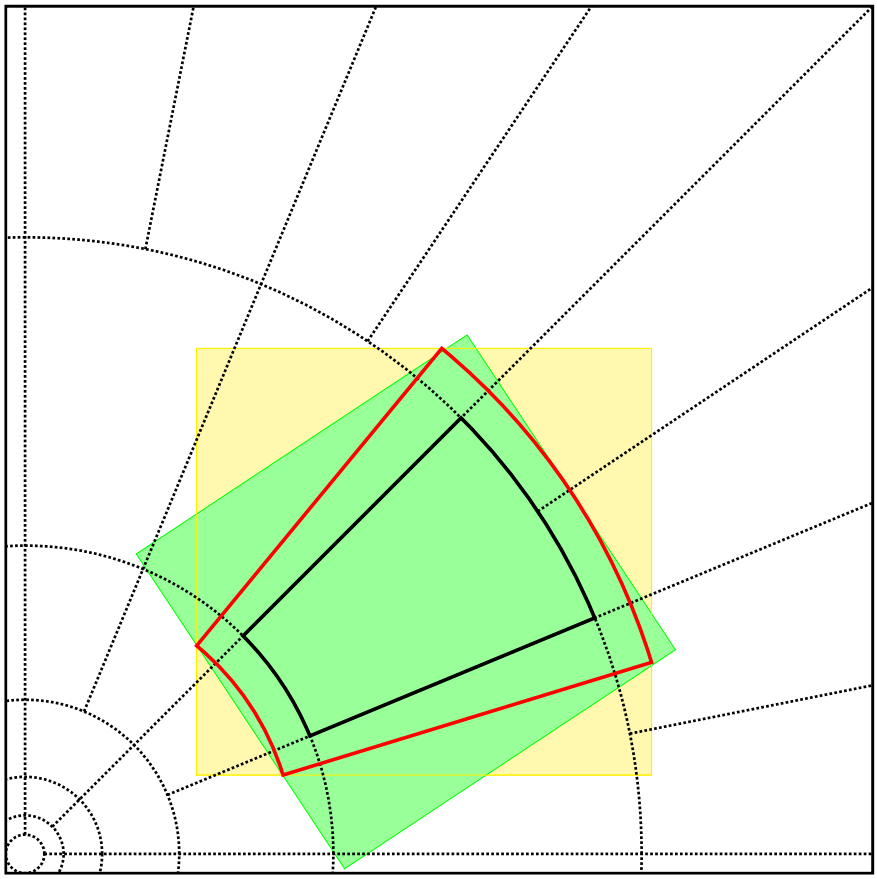

Figure 3.5: Comparison between smallest axial aligned rectangle (yellow) and smallest rectangle in curvelet direction (green) for one representative curvelet. Support of the considered curvelet shown in red. Only the first quadrant of the Fourier plane is shown.

The source of this problem is the fact, that the rectangle we want to transform back using IFFT needs to be axial aligned. In the following we introduce a method providing a minimal number of

coefficients for each curvelet independent of its direction. The basic idea is the so called wrapping, introduced by Candès et. al. in [2], but modified to fit our curvelet tiling. It consists of three steps:

- Firstly we compute the smallest rectangle containing the support of a curvelet $\hat{\Psi}$.
- In a second step we will extend the rectangle to the whole Fourier plane by periodisation in a particular manner
- Finally, we choose an axial aligned rectangle of suitable size and centered around the origin, containing all information. This rectangle will then be used for the inverse Fast Fourier transformation.

3.3.1 Computation of the smallest rectangle

In order to determine the smallest rectangle S surrounding the support of a wedge, we derive the surface area in dependency of the (minimal) angle α between the rectangle side a and the wedge side w for any wedge support width angle σ. The labeling can be found in Fig.3.6. (The angle α is considered to be zero if the lines are parallel.) For a given α the directions of all sides of the rectangle

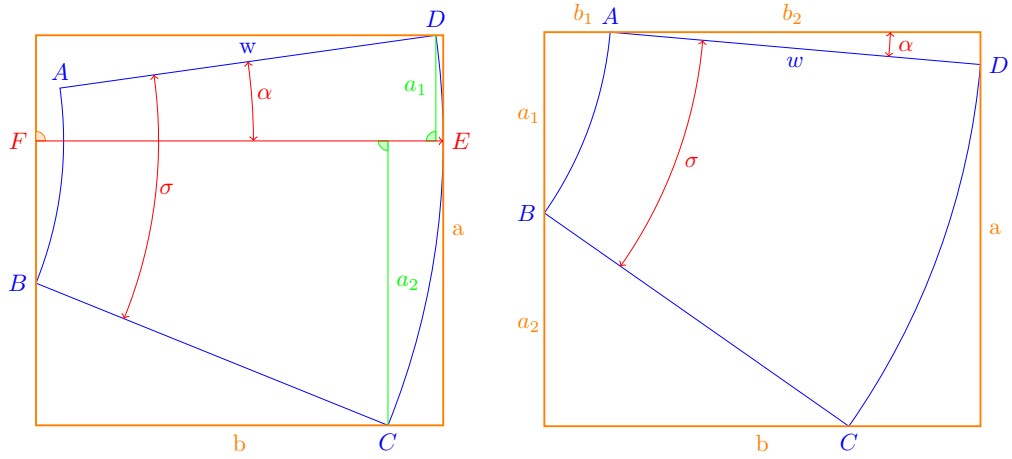

(a) $\alpha < 0$, angle within curvelet support

(b) $\alpha > 0$, angle outside curvelet support

Figure 3.6: Sketch of the smallest rectangle with direction α, containing the support of a given wedge.

are fixed and therefore the smallest rectangle for that direction is the rectangle, whose sides touch the wedge, but do not subtend it. Without loss of generality only $\alpha \in [\frac{\pi}{2} - \sigma, \sigma/2]$ have to be considered because of the symmetry of the wedge and the fact, that α and $\alpha + \frac{\pi}{2}$ yield the same rectangle.

Two cases have to be distinguished: For $\alpha \leq 0$ the line a touches the arc t tangentially at a point $E \notin \{C, D\} \forall \alpha \neq 0$. For $\alpha > 0$ the line a touches the arc t in the point D non tangentially.

Let us first consider the case $\alpha \leq 0$: Simple trigonometric arguments lead to

$$\begin{aligned} A(\alpha) &= a \cdot b = (a_1 + a_2) \cdot (2r - F_x) \\ &= (2r\sin(-\alpha) + 2r\sin(\sigma + \alpha)) \cdot (2r - r\cos(\sigma + \alpha)) \\ &= 2r^2 \cdot (\sin(-\alpha) + \sin(\sigma + \alpha)) \cdot (2 - \cos(\sigma + \alpha)). \end{aligned} \tag{3.7}$$

For $\alpha \geq 0$ we derive

$$\begin{aligned} A(\alpha) &= a \cdot b = (a_1 + a_2) \cdot (b_1 + b_2) \\ &= \left(\overline{AB}\cos(\alpha + \frac{\sigma}{2}) + r\sin(\alpha + \sigma)\right) \cdot \left(r\cos(\alpha) + \overline{AB}\sin(\alpha + \frac{\sigma}{2})\right) \\ &= r^2 \cdot \left(\frac{\cos(\alpha + \frac{\sigma}{2}) \cdot sin(\sigma)}{\sin(\frac{\pi}{2} - \frac{\sigma}{2}))} + \sin(\alpha + \sigma)\right) \cdot \left(\cos(\alpha) + \frac{\sin(\alpha + \frac{\sigma}{2}) \cdot \sin(\sigma)}{\sin(\frac{\pi}{2} + \frac{\sigma}{2})}\right). \end{aligned} \tag{3.8}$$

A plot of $A(\alpha)$ can be seen in Fig.3.7. As a next step, the derivative $\frac{dA(\alpha)}{d\alpha}$ is computed:

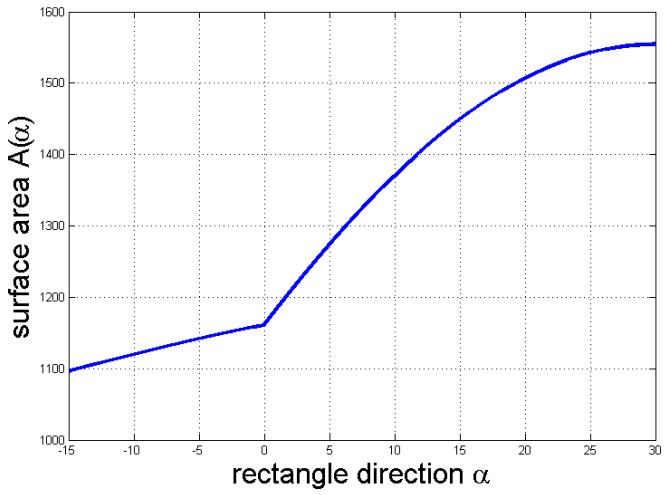

Figure 3.7: Plot of the surface area $A(\alpha)$ in dependency of the rectangle direction α for parameters $\sigma = 30°$, $r = 2^5$.

$$\begin{aligned} \frac{dA(\alpha)}{d\alpha} &= 2r^2[(sin(-\alpha) + \sin(\sigma + \alpha)) \cdot (-\sin(\sigma + \alpha)) \\ &\quad + (\cos(\alpha) - \cos(\sigma + \alpha)) \cdot (2 - \cos(\sigma + \alpha))] \end{aligned} \tag{3.9}$$

Especially interesting are the points $\alpha = 0$ and $\alpha = -\frac{\sigma}{2}$:

$$\frac{dA}{d\alpha}(-\frac{\sigma}{2}) = 2r^2\left(2\sin^2(\frac{\sigma}{2}) + 0\right) = 4r^2\sin^2(\frac{\sigma}{2}) > 0 \tag{3.10}$$

This shows that we have an at least local minimum for $\alpha = -\frac{\sigma}{2}$. Now we take a look at $alpha = 0$:

$$\begin{aligned}
\frac{dA}{d\alpha}(0) &= 2r^2\left(sin^2(\sigma) + (-1+\cos(\sigma))\cdot(2-\cos(\sigma))\right) \\
&= 2r^2\left(sin^2(\sigma) - 2 + \cos(\sigma) + 2\cos(\sigma) - \cos^2(\sigma)\right) \\
&= 2r^2\left(-2 + 3\cos(\sigma) + sin^2(\sigma) + \cos^2(\sigma) - 2\cos^2(\sigma)\right) \\
&= 2r^2\left(-1 + 3\cos(\sigma) - 2\cos^2(\sigma)\right) \\
&= 2r^2\left(-1 + \cos(\sigma) - 2\cos(\sigma)(-1+\cos(\sigma))\right) \\
&= 2r^2\underbrace{(-1+\cos(\sigma))}_{<0}(1-2\cos(\sigma)) = \begin{cases} <0 & \text{if } \sigma > \frac{\pi}{3}, \\ >0 & \text{if } \sigma < \frac{\pi}{3}. \end{cases}
\end{aligned} \tag{3.11}$$

Additionally one can show $A(0) > A(-\frac{\sigma}{2})$ for any $0 < \sigma \leq \frac{\pi}{2}$:

$$\begin{aligned}
A(0) - A(-\frac{\sigma}{2}) &= 2\underbrace{\sin\sigma}_{=2\sin\frac{\sigma}{2}\cos\frac{\sigma}{2}} - \underbrace{\sin\sigma\cos\sigma}_{=2\sin\frac{\sigma}{2}\cos\frac{\sigma}{2}(1-2\sin^2\frac{\sigma}{2})} - 4\sin\frac{\sigma}{2} + 2\sin\frac{\sigma}{2}\cos\frac{\sigma}{2} \\
&= 4\sin\frac{\sigma}{2}\left(\cos\frac{\sigma}{2} - \underbrace{1}_{=sin^2\frac{\sigma}{2}+\cos^2\frac{\sigma}{2}} + \cos\frac{\sigma}{2}\sin^2\frac{\sigma}{2}\right) \\
&= \underbrace{4\sin\frac{\sigma}{2}}_{>0}\underbrace{\left(1-\cos\frac{\sigma}{2}\right)}_{>0}\underbrace{\left(\cos\frac{\sigma}{2} - \sin^2\frac{\sigma}{2}\right)}_{>0, \text{ for } 0<\sigma\leq\frac{\pi}{2}} > 0
\end{aligned} \tag{3.12}$$

This leads to the following Proposition:

Proposition: Assuming no minimums for $\alpha \in (-\frac{\sigma}{2}, 0)$, the surface area $A(\alpha)$ reaches its minimum at $\alpha = -\frac{\sigma}{2}$.

This shows that the rectangle R in curvelet direction is the smallest rectangle surrounding the support of a given wedge.

3.3.2 Periodisation: Extension to the whole Fourier plane

Now that we have computed the smallest rectangle, containing the complete support we extend this rectangle by periodisation in a special manner: Firstly, the rectangle is extended along the axis of the rectangle side, which is perpendicular to the curvelet direction. In a second step the resulting stripe is extended in x-axis direction. Note that these two periodisation axes are (in general) not perpendicular and therefore neighboring stripes look shifted to each other, as can be seen in Fig.3.8. The reason for this kind of periodisation can be seen in the next section.

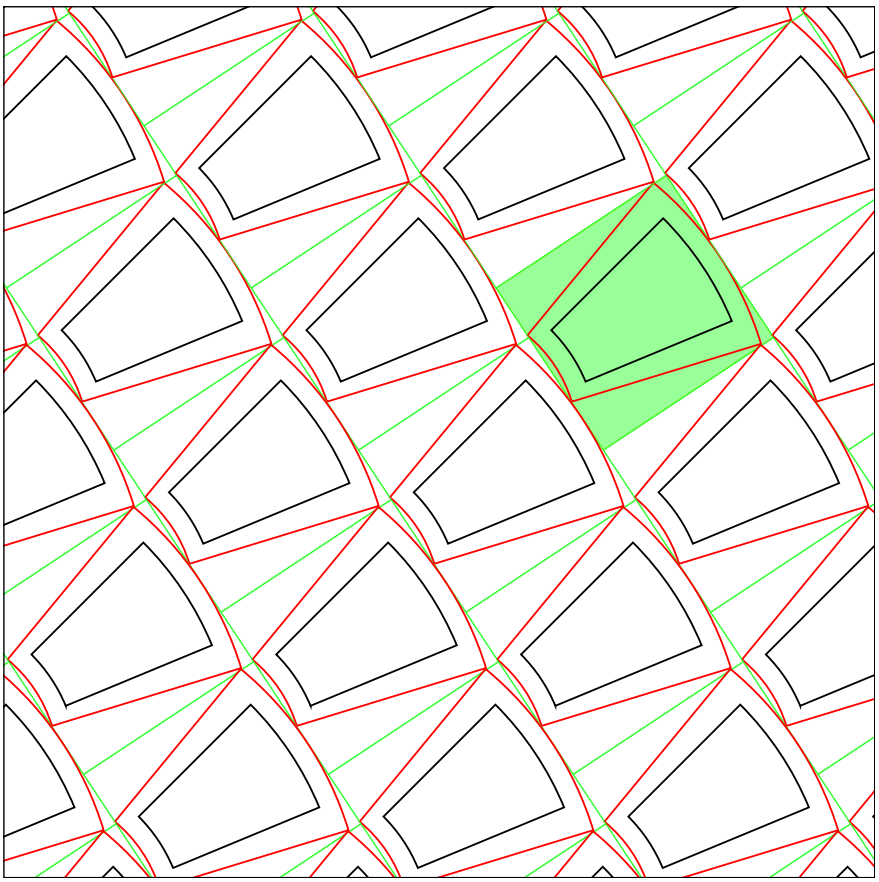

Figure 3.8: Periodisation of the rectangle S, shown in green, like described in Subsection 3.3.2.

3.3.3 Computation of the wrapping window

In this step our aim is to compute a rectangle, centered around the origin, with the smallest possible size but containing all information. It is obvious, that the rectangle must at least have the same surface area as the rectangle computed in step 1. We will see that this lower bound can be reached. In the following we only consider the case of a curvelet in the Fourier sector East or West. Other sectors follow analog. We already know the width b and length l of the rectangle S, containing the support of the considered curvelet. The rectangle W of width $\hat{b} = \frac{b}{\cos\alpha}$ and length $\hat{l} = l\cos\alpha$ has the same surface area. You can find a sketch of this transformation in Fig.3.9. The interesting part is, that if W is placed on the periodised Fourier plane, it always contains each pixel of the original wedge, independently of the location of W. As depicted in Fig.3.10, only the location of a pixel in relation to W changes. This corresponds to a relabeling of the pixels. For simplicity we will always center the wrapping window W around the origin. This rectangle W is used to represent the product $(\hat{f} \cdot \hat{\Psi}_{j,l,\cdot})[n_1, n_2]$. But why is this useful?

The interesting point is, this small rectangle can be used for the backprojection using the inverse Fourier transform, and during syntheses the relabeling can easily be inverted: As we know that the

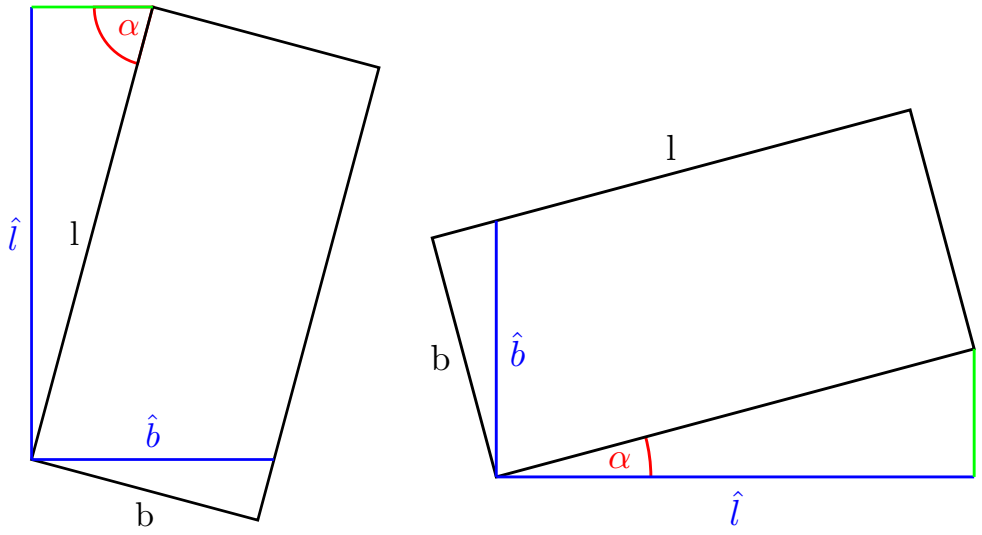

(a) North and South of Fourier plane (b) East and West of Fourier plane

Figure 3.9: Sketch of the determination of the wrapping window size

rectangle W was centered and the size of the original image is known, we can extend W by periodisation over the Fourier plane of size $n \times n$. We also know where the support of the corresponding curvelet is located. We can compute the location of S and drop the data outside. Doing this, we retrieve the original product $(\hat{f} \cdot \hat{\Psi}_{j,l,\cdot})[n_1, n_2]$.

In fact the computation of the wrapping window is only motivated in this way. The actual computation is done in an opposite way. Instead of the periodisation of the data, meaning the product $(\hat{f} \cdot \hat{\Psi}_{j,l,\cdot})[n_1, n_2]$, the position of the wrapping window is translated in a sufficient, periodic way, sketched in Fig.3.11. These translates are then summed up. This is easier to do and fits very well with the representation of a curvelet elaborated in section 3.2, as we only have to consider translates subtending the rectangle R. Every translate of the original wrapping window is computed in a way that each wrapping window would contain the same information if laid over the periodisation of the smallest rectangle. This guarantees, that the sum over the data (not the periodisation of the data,) contains exactly the same as the original wrapping window.

To put this in mathematical terms we first derive the number of vertical stripes. This reads at most $2\lceil \frac{n-\hat{a}}{2}/\hat{a} \rceil + 1$, meaning a centered stripe and on both, the left and the right side, a number of $\lceil \frac{n}{2} - \frac{\hat{a}}{2} \rceil$ stripes. Therefore the horizontal index reads $i \in \{1, \ldots, 2\lceil \frac{n-\hat{a}}{2}/\hat{a} \rceil + 1\}$. Analog the vertical index reads $j \in \{1, \ldots, 2\lceil \frac{n-\hat{b}}{2}/\hat{b} \rceil + 1\}$. In a next step we have to calculate the horizontal shift from one vertical stripe to another. The shift is the difference of the left and right lower points of the rectangle S, and hence, reads $s = |D_y - C_y| = \lceil \frac{b}{\sin \alpha} \rceil$. Now we can define the single wrapping windows:

$$W_{i,j}(x, y) = \left(\hat{f} \cdot \hat{\Psi}_{j,l,\cdot}\right)[b_{i,j} + (x, y)], \tag{3.13}$$

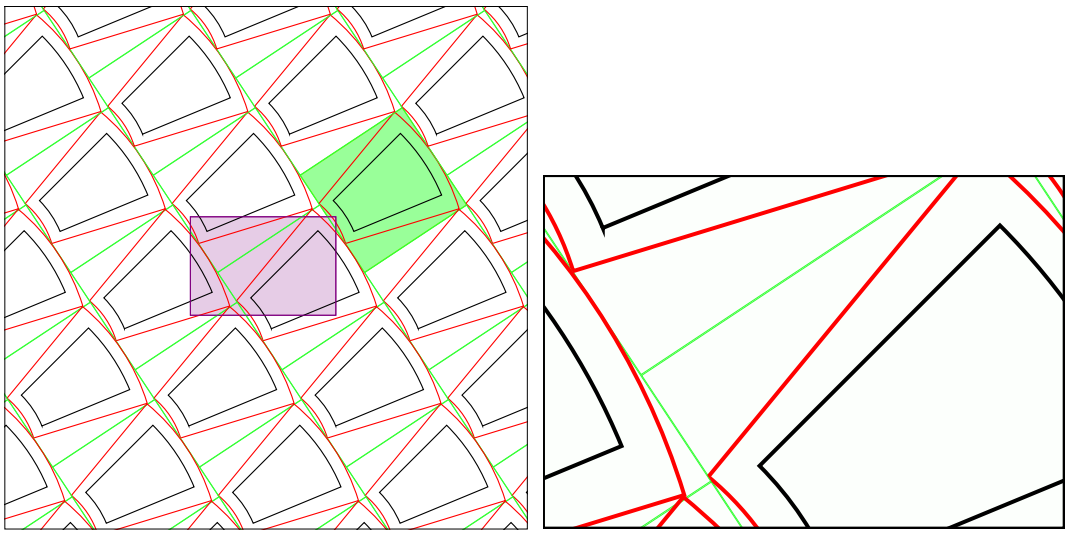

(a) Periodisation and location of the wrapping window (b) Zoom of resulting wrapping window

Figure 3.10: Periodisation of the smallest rectangle in curvelet direction (green) and corresponding wrapping window (violet).

where

$$
\begin{aligned}
b_{i,j} &= b_j + (i-1) * (0, \hat{a}), \\
b_j &= b_0 + ((j-1) * \hat{b}, (j-1) * s - \lceil \frac{(j-1) * s}{s} \rceil \cdot s), \\
b_0 &= (\lceil \frac{n}{2} - \frac{\hat{b}}{2} - \frac{n-\hat{b}}{2} \rceil, (\frac{n}{2} - (\frac{n-\hat{b}}{2} / \hat{b}) \cdot \hat{a}) - \lceil \frac{\frac{n}{2} - (\frac{n-\hat{b}}{2} / \hat{b}) \cdot \hat{a}}{\hat{b}} \rceil \cdot \hat{b}).
\end{aligned}
\tag{3.14}
$$

Here, b_0 is the left upper corner of the first window, the window containing the point $(0,0)$. The point b_j denotes the left upper corner of the j-th stripe and finally the point $b_{i,j}$ is the left upper corner of the i-th window in the j-th stripe. With these notations, the resulting wrapping window reads

$$
W(x,y) = \sum_{i,j} W_{i,j}(x,y) \text{ for } x = 1, \cdots, \hat{b}, y = 1, \cdots, \hat{a}. \tag{3.15}
$$

Again these formulations only holds true for the East region of the image, the decomposition of the other regions is performed an analogous manner.

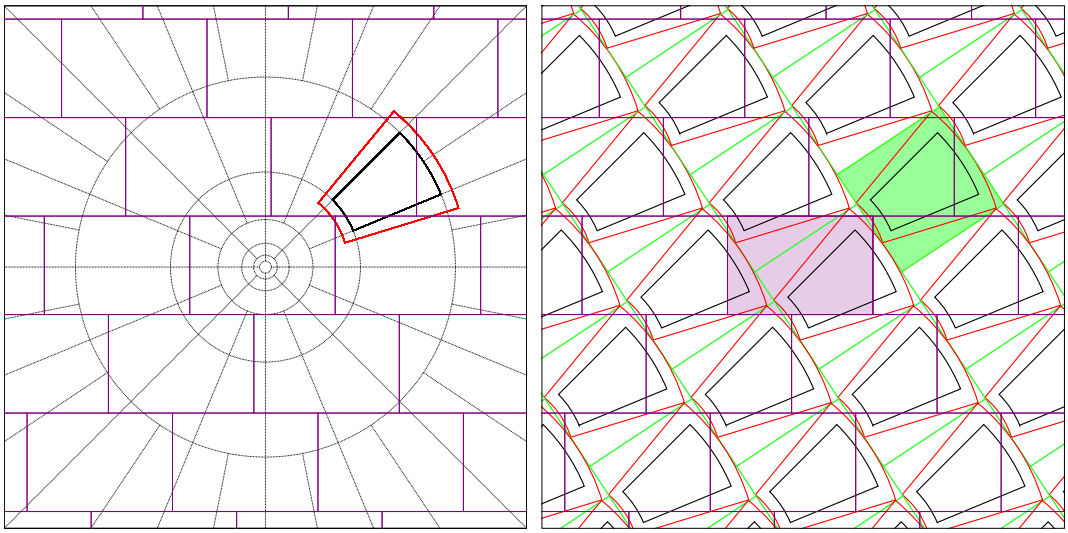

(a) Periodisation of the wrapping window

(b) Periodisation of the wrapping window laid over the periodisation of the rectangle S

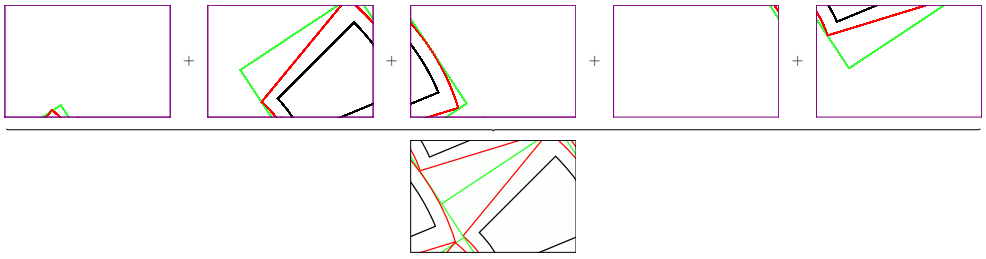

(c) Composition of the wrapping window by addition

Figure 3.11: Sketch of the computation of the wrapping window by periodisation and addition of all windows.

3.4 Final Algorithm

In the above sections we have discussed some major drawbacks of the initial algorithms presented at the beginning of this chapter. We were able to resolve problems causing unnecessary long computational time in the calculation of single curvelets. This resulted in a significant speed up of the transform. Moreover we reduced the sampling of curvelets in spatial domain by introducing a wrapping window method. This lead to less redundancy in the corresponding frame and hence, agrees better with the definitions of the sampling introduced in Section 1.2 in the continuous case. Now we are able to present the final algorithm using the elaborated results.

3.4.1 Analysis Algorithm

We supplement the initial analysis algorithm introduced in section 3.1 with the enhancements shown in Section 3.2 and Section 3.3.

The analysis operator $\mathfrak{A} : \Omega \mapsto \mathbb{C}^p$, $\mathfrak{A}f = \{\langle f, \Psi_{j,l,k}\rangle\}_{j,l,k}$ described in Chapter 1.2 is to be implemented. For a given image image $f[n_1, n_2]$, $0 < n_1, n_2 \leq n$, a set of coefficients $c_{j,k,l}$ is computed.

1. Firstly we compute the 2D-FFT $\hat{f}[n_1, n_2]$.
2. For each radial and angular scale $\{j, l\}$ we compute the curvelet $\hat{\Psi}_{j,l,\cdot}[n_1, n_2]$ in Fourier domain for $x_{min} \leq n_1 \leq x_{max}$, $y_{min} \leq n_2 \leq y_{max}$ with $x_{min}, x_{max}, y_{min}, y_{max}$ according to section 3.2.
3. Now the point-wise product $\hat{v}[n_1, n_2] = \hat{f}[n_1, n_2] \cdot \hat{\Psi}_{j,l,\cdot}[n_1, n_2]$ is calculated for $x_{min} \leq n_1 \leq x_{max}$, $y_{min} \leq n_2 \leq y_{max}$.
4. The wrapping window $\hat{W}[x, y]$ is computed in Fourier space according to Eq.(3.15).
5. The 2D-IFFT yields the coefficient matrix $c_{j,l,k} = W[k_1, k_2]$ for $0 < k_1 \leq \hat{l}$, $0 < k_1 \leq \hat{b}$ for sectors East and West and $0 < k_1 \leq \hat{b}$, $0 < k_1 \leq \hat{l}$ for sectors North and South.

3.4.2 Synthesis Algorithm

The synthesis of the upper analysis algorithm consists again of executing the inverse of each step in a different order.

5'. The 2D-FFT of the coefficient matrix $c_{j,l}$ is computed and $\hat{W}[k_1, k_2]$ derived.

4'. The window is unwrapped by periodisation: $\tilde{W}(n_1, n_2) = \hat{W}(n_1 - \lceil \frac{n_1}{\hat{a}} \rceil \cdot \hat{a} - \frac{\hat{a}}{2}, n_2 - \lceil \frac{n_2}{\hat{b}} \rceil \cdot \hat{b} - \frac{\hat{b}}{2})$ for $x_{min} \leq n_1 \leq x_{max}$, $y_{min} \leq n_2 \leq y_{max}$.

2'. For each radial and angular scale (j,l) we compute the curvelet $\hat{\Psi}_{j,l,\cdot}[n_1, n_2]$ in Fourier domain for $x_{min} \leq n_1 \leq x_{max}$, $y_{min} \leq n_2 \leq y_{max}$ with $x_{min}, x_{max}, y_{min}, y_{max}$ according to section 3.2.

3'. Now the point-wise product $\hat{v}_{j,l}[n_1, n_2] = \tilde{W}[n_1, n_2] \cdot \hat{\Psi}_{j,l,\cdot}[n_1, n_2]$ is calculated for $x_{min} \leq n_1 \leq x_{max}$, $y_{min} \leq n_2 \leq y_{max}$.

1'. At last we compute the inverse 2D-IFFT of the sum of the products $\sum_{j,l} \hat{v}_{j,l}[n_1, n_2]$ and obtain $f[n_1, n_2]$.

Note that between step [4'] and step [3'] the periodised wrapping window $\tilde{W}$ is not set to zero outside the curvelet support, as this takes place automatically in the formulation as the product $\hat{v}[n_1, n_2] = \tilde{W}[n_1, n_2] \cdot \hat{\Psi}_{j,l,\cdot}[n_1, n_2]$.

3.4.3 Discussion

The analysis and synthesis algorithm derived in this chapter guarantee a fast computation of the curvelet coefficients $c_{j,l,k}$. The curvelets are downsampled in an optimal way, and hence the corresponding frame has as few redundancy as possible.

3.5 Comparison to the discrete Curvelet Transformation proposed by Candès et.al.

In the following we want to elaborate differences in the implementation of our fast discrete curvelet transform and the one proposed in [2]. For each difference we will state advantages, disadvantages as well as the motivation for each particular ansatz. Both attempts have their eligibility, as they aim on different applications and are optimized for the usage in this field.

The digital transform by Candès et. al. aim on the representation of images in terms of the curvelet frame. They direct their attention to the adaption to the discrete grid. This simplifies and hence accelerates the computation, but leads to less conformity to the continuous definitions of the curvelet transform.

In contrast to that, our implementation treats two aspects: On the one hand side, we want to stick to the continuous definitions as much as possible. On the other hand side, more importantly we want to be able to modify the tiling of the Fourier plane in order to adapt the transform for the use (in reconstruction methods) in limited angle tomography.

The most fundamental difference between the two implementations is the use of other tilings of the Fourier plane. All of the following differences are direct consequences of this conceptional distinction.

Instead of concentric circles, Candès et.al. use squares to divide the plane into different radial scales. (Moreover the radial scales are divided not by equispaced angles but equispaced slopes. But this is of no further consequence.) This so called “Cartesian coronae” results in more shear-shaped wedges in comparison to their continuous analogue and our implementation. A scheme of the tiling is depicted in Fig.3.12.

The usage of this specific tiling is motivated by the discrete representation of images itself and brings along some advantages. It is very convenient, as it simplifies the implementation of the window functions $W(r)$ and $V(\omega)$. Moreover the wedges are nearly parallelograms and therefore it is easy to find the smallest parallelogram P containing the support of one wedge. These parallelograms simplify the computation of the wrapping window in a great measure. In addition to that the parallelogram P contains less values outside the support of these curvelets than our smallest rectangle S in section 3.3.1 does. This leads to even less redundancy in the curvelet representation of an image.

The use of our tiling is motivated by it’s total conformity to the continuous case. All wedges are uniformly shaped and independent of their angular direction. This is especially useful as soon as we consider a limited angular range like in the tilings presented in Chapter 2.

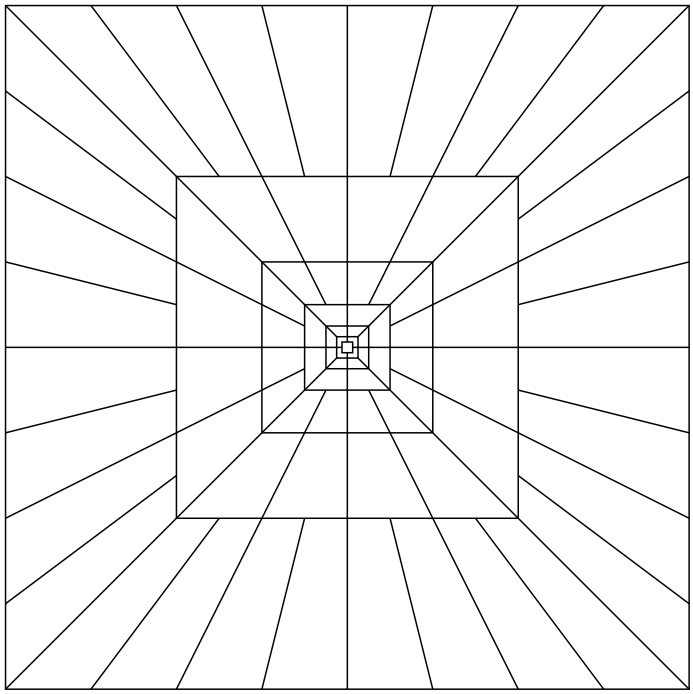

Figure 3.12: Discrete tiling of the Fourier space: “Cartesian coronae”.

4 Numerical Results

During this thesis we have considered the reconstruction problem

$$\hat{c} = \underset{c \in \mathbb{R}^N}{\arg\min} \left\{ \frac{1}{2} \|Kc - y^\delta\|^2_{L^2(S^1 \times \mathbb{R}} + \|c\|_{1,w} \right\}, \tag{4.1}$$

and stated the soft-thresholding algorithm for this problem in Section 1.3. Moreover, we adapted the curvelet transform to fit to the limited angle data acquisition. This was accomplished by the use of different tilings of the Fourier plane. Now, in the present chapter we briefly review the parts of the previous chapters that are important for the numerical experiments. We state the different parameters values we are able to choose, i.e. the curvelet tiling or the initial value we use. Finally, we present the resulting images, inspect them and evaluate them visually. Hereby, we give possible explanations for each observation we make. In the end, we work out which parameters leads to the best solution to our reconstruction problem.

4.1 Phantoms for numerical experiments

For the numerical experiments we use the Shepp-Logan head phantom with improved contrast and a white circle on black background for the comparison of the numerical results. Both phantoms are depicted in Fig. 4.1 .

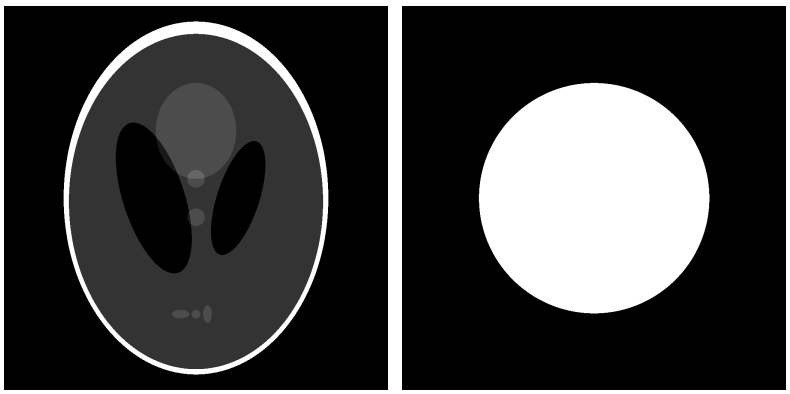

(a) Shepp-Logan head phantom (b) White circle

Figure 4.1: The phantoms used for the numerical experiments in this chapter.

4.2 The different Curvelet tilings

The following curvelet tilings are used:

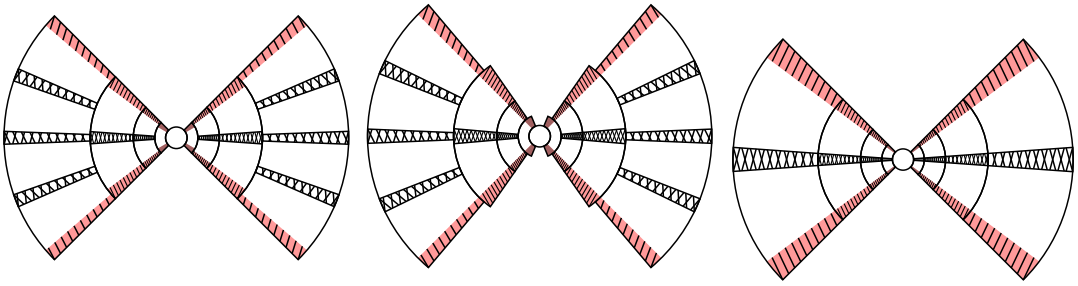

(a) Inner Fading (b) Outer Fading (c) Uniform Fading

Hereby, both Uniform Fadings, the Inner Uniform Fading and the Outer Uniform Fading, are used. For details and the construction of the different tilings we refer to Chapter 2.

4.3 The Initial Value

We consider the following three initial values for the numerical reconstruction:

- ZERO: A black image is used.
- FBP: The filtered backprojection of the measured data is used. The missing angles are extended by zero-padding
- SFBP: A smoothed filtered backprojection of the measured data is used. Here, also the missing angles are extended by zero-padding. Additionally the measurement data is manipulated. In order to smooth the cut-off between measured angles and not measured angles, the measurements are weighted according to the distance to the limited angle. After that the manipulated data is backprojected. This reduces some artifacts in the initial image, as can be seen in Fig. 4.2.

Both, the FBP and the SFBP are very noise sensitive and therefore despite their good results in absence of noise are not suited for practical application. Note that, as we are interested in reconstructing the curvelet coefficients $\hat{c}_{j,l,k}$ the initial value is also given in form of the curvelet transform of the above discussed initial images.

4.4 The Reconstruction Algorithm

For the reconstruction process a modified version of the iterated soft-thresholding algorithm discussed in Section 1.3 is used. An additional step size control was added to assure descent of the

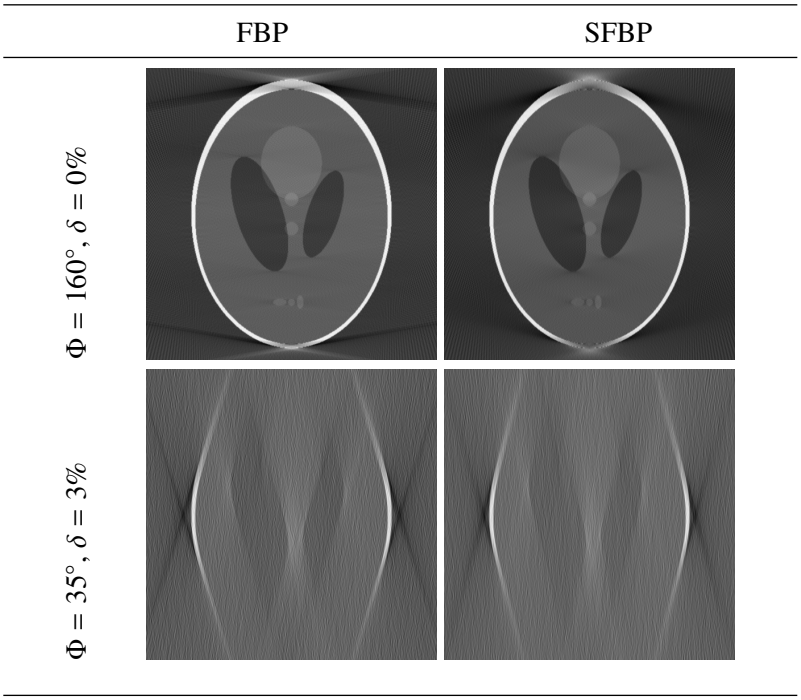

Figure 4.2: Comparison of the initial values FBP and SFBP with noise level 3% and in absence of noise.

model error in every iteration: After computing an iteration step, the resulting image and residuum is computed. The step is accepted only if the residuum is smaller than the residuum of the last iteration step. If not, the step size is assumed to be too large and hence is decreased by a factor $f < 1$. We use $f = 1/2$. With this smaller step size the current iteration is repeated. If the step size is accepted it is increased in the next iteration by the factor $\frac{1}{f} > 1$ in order to prevent unnecessary small step sizes in iterations after necessary small steps. This decrease and increase of the step size is limited by a lower and upper step size bound s_{min}, resp. s_{max}. Algorithm 1 implements this procedure.

During the experiments the following parameter values are used: $c_0 = 0$, $\tau_{j,k,l}$ according to (1.30), $s_{min} = 10^{-10}$, $s_{max} = 10^{10}$, $n_{max} = 1000$, $f = 1/2$ if not stated otherwise.

4.5 Numerical Results

In the following we present the numerical results and afterwards discuss our observations. We present the reconstructed images for the four different tilings Inner Fading, Outer Fading, Inner Uniform Fading, Outer Uniform Fading; the three different initial values ZERO, FBP, SFBP; the limited angle $\Phi \in \{35, 160\}$; the noise level $\delta \in \{0, 0.03\}$. The parameters $n_{max} = 1000$, $s_{min} = 10^{-10}$, $s_{max} = 10^{10}$, $f = 1/2$ were used. The resulting images can be found in Figures 4.3 to 4.10.

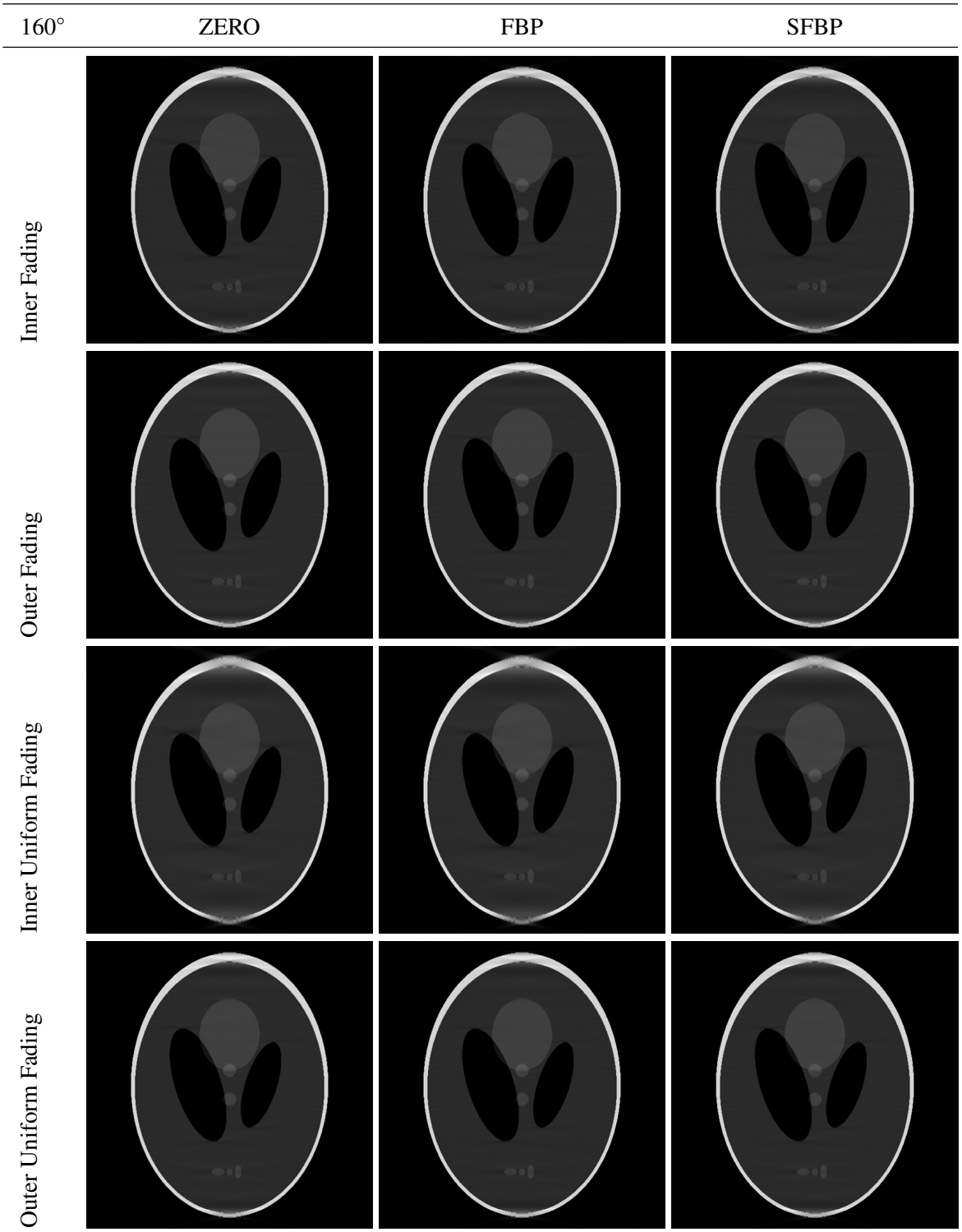

Figure 4.3: Reconstruction of the Shepp-Logan head phantom of size 512 x 512 without presence of noise, limited angle $\Phi = 160°$. Reconstructions for the initial values ZERO, FBP and SFBP, and Curvelet tilings Inner Fading, Outer Fading, Inner Uniform Fading, Outer Uniform Fading are shown.

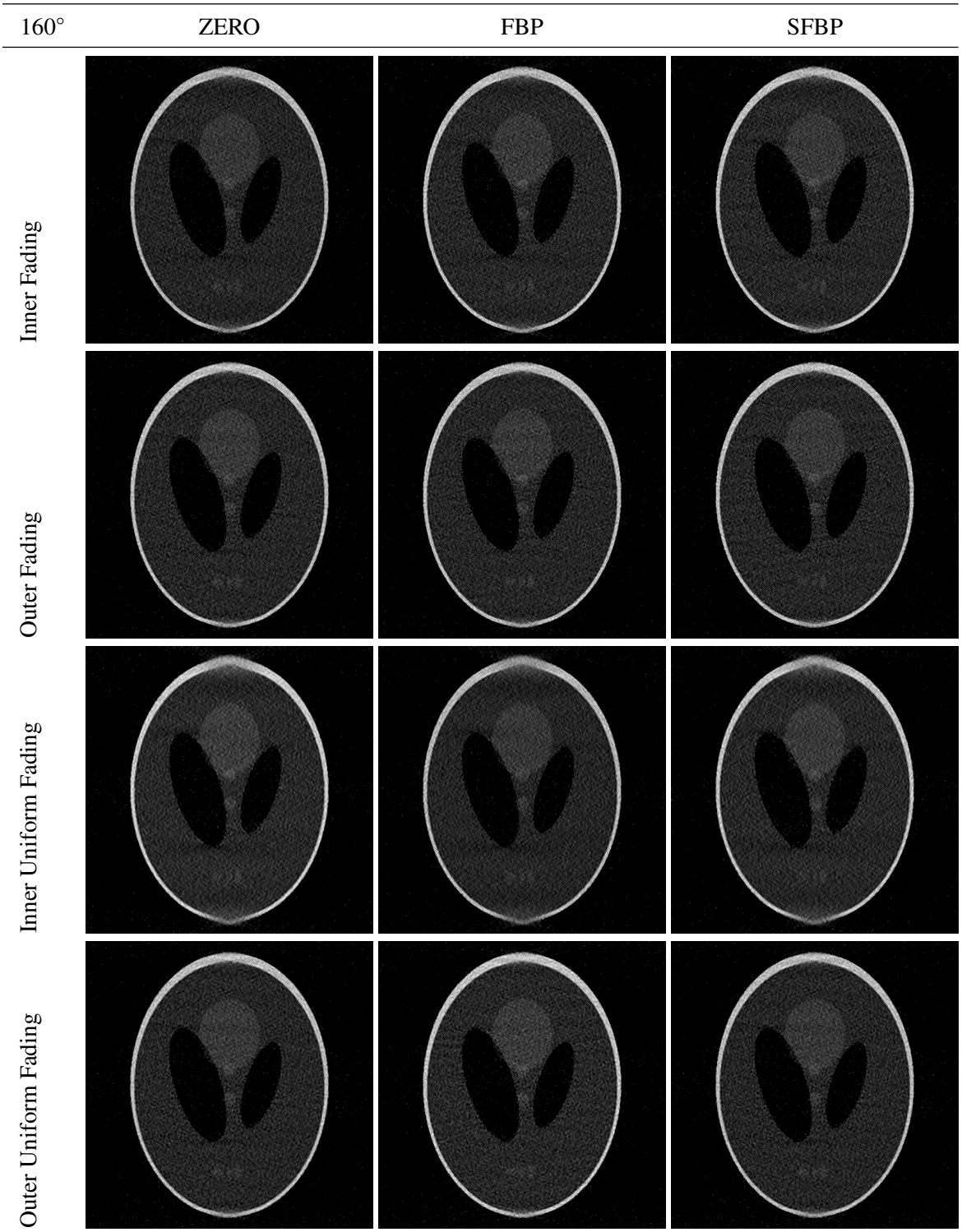

Figure 4.4: Reconstruction of the Shepp-Logan head phantom of size 512 x 512 without presence of noise, limited angle $\Phi = 160°$. Reconstructions for the initial values ZERO, FBP and SFBP, and Curvelet tilings Inner Fading, Outer Fading, Inner Uniform Fading, Outer Uniform Fading are shown.

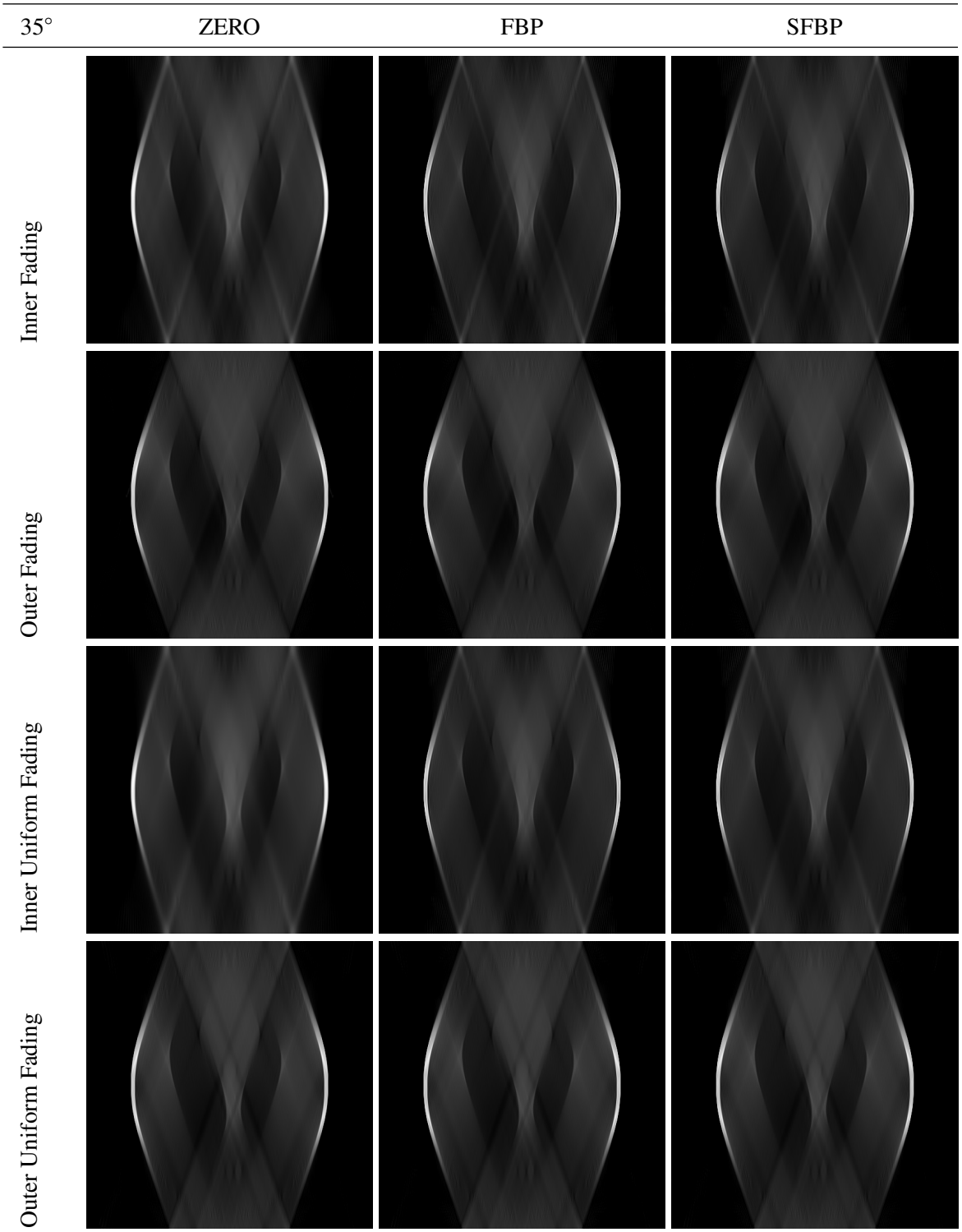

Figure 4.5: Reconstruction of the Shepp-Logan head phantom of size 512 x 512 without presence of noise, limited angle $\Phi = 35°$. Reconstructions for the initial values ZERO, FBP and SFBP, and Curvelet tilings Inner Fading, Outer Fading, Inner Uniform Fading, Outer Uniform Fading are shown.

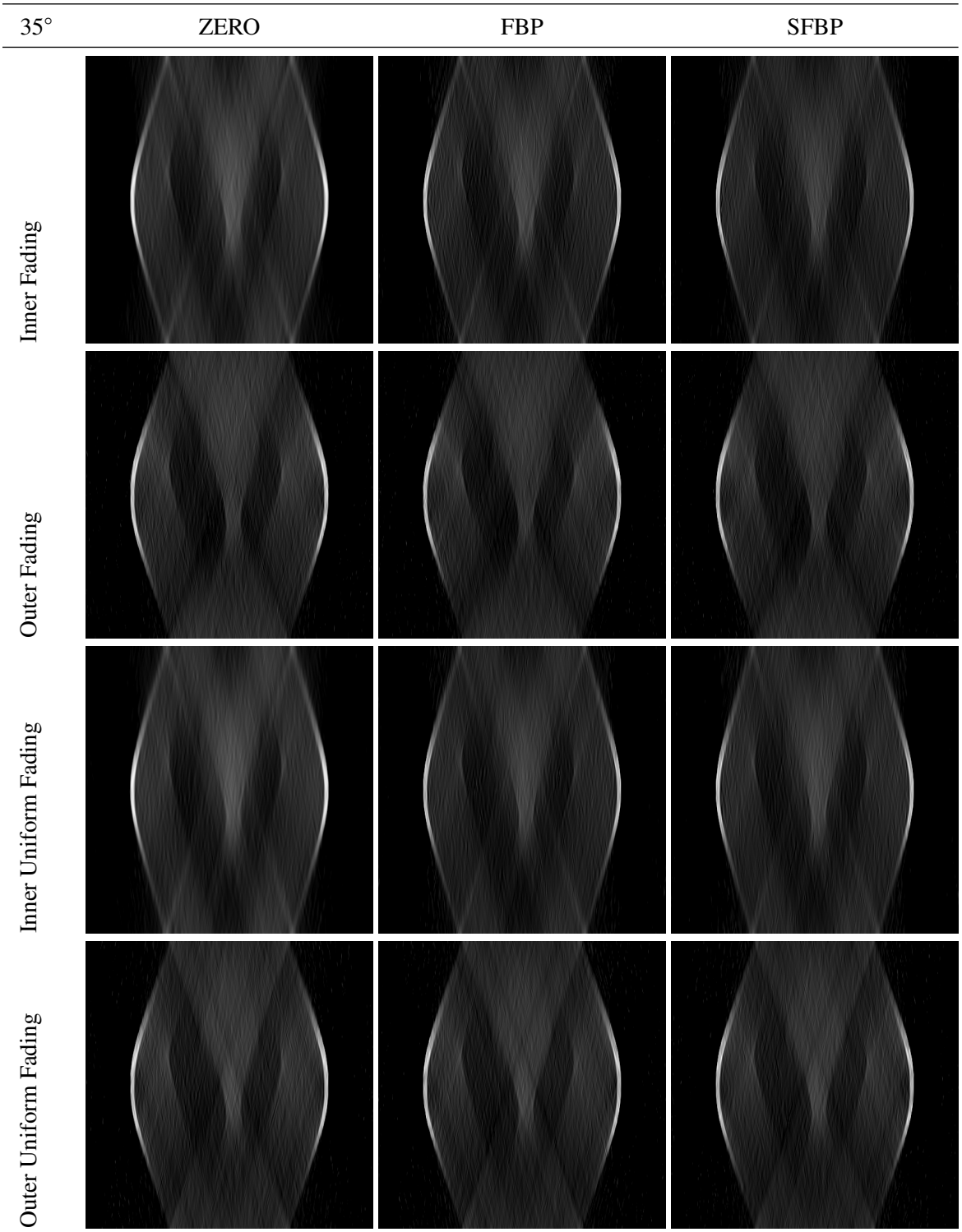

Figure 4.6: Reconstruction of the Shepp-Logan head phantom of size 512 x 512 without presence of noise, limited angle $\Phi = 35°$. Reconstructions for the initial values ZERO, FBP and SFBP, and Curvelet tilings Inner Fading, Outer Fading, Inner Uniform Fading, Outer Uniform Fading are shown.

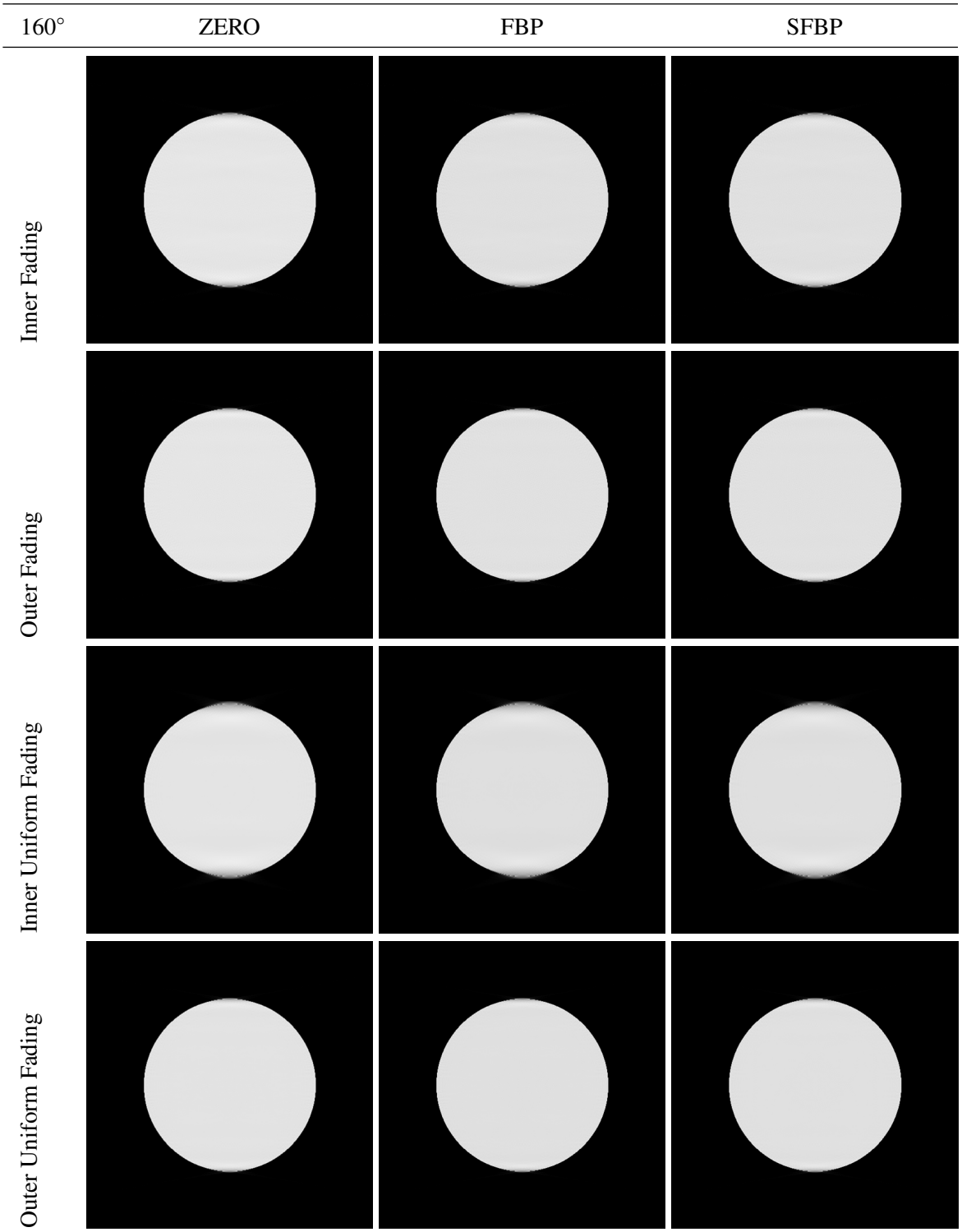

Figure 4.7: Reconstruction of the ball of size 512 x 512 without presence of noise, limited angle $\Phi = 160°$. Reconstructions for the initial values ZERO, FBP and SFBP, and Curvelet tilings Inner Fading, Outer Fading, Inner Uniform Fading, Outer Uniform Fading are shown.

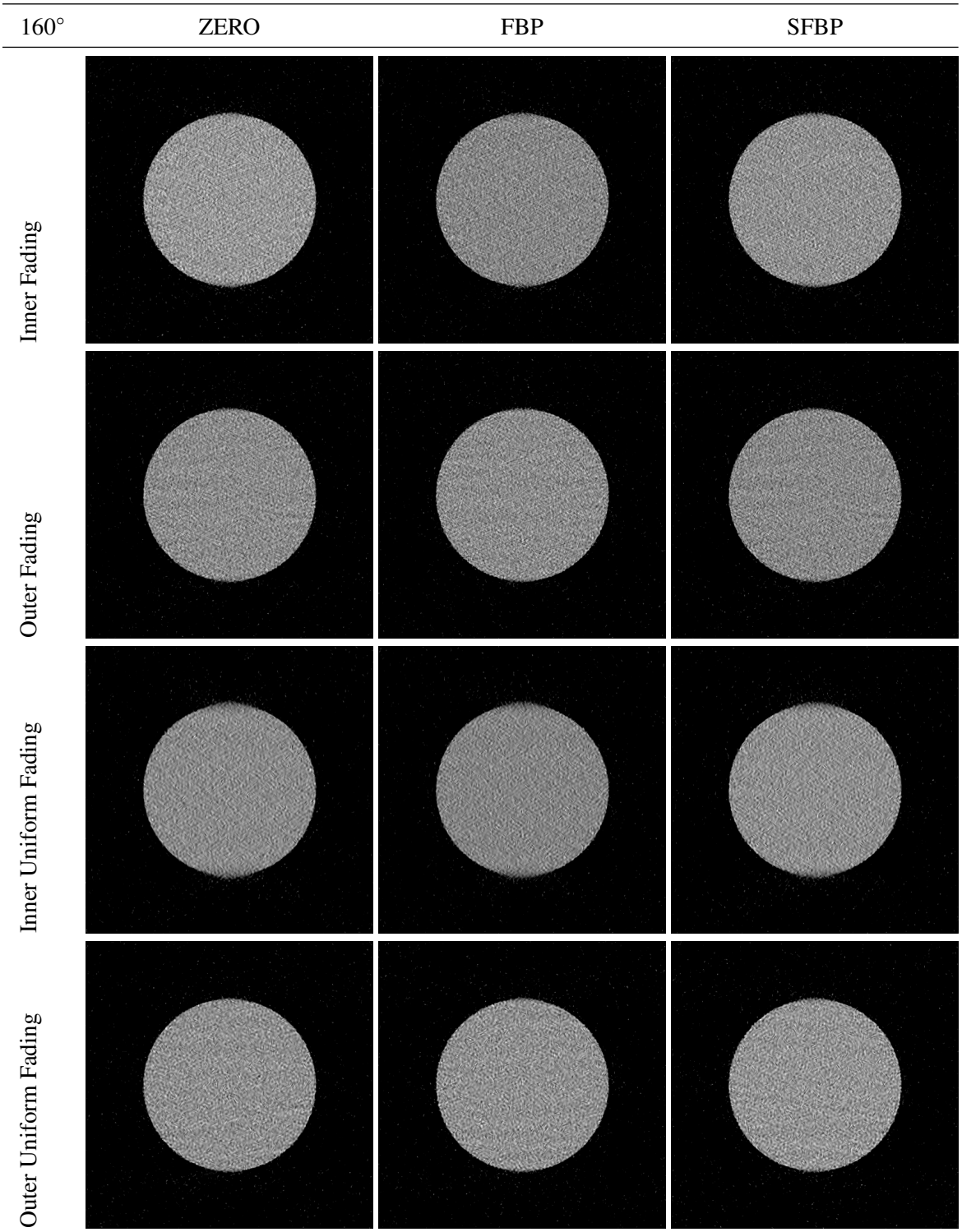

Figure 4.8: Reconstruction of the ball of size 512 x 512 without presence of noise, limited angle $\Phi = 160°$. Reconstructions for the initial values ZERO, FBP and SFBP, and Curvelet tilings Inner Fading, Outer Fading, Inner Uniform Fading, Outer Uniform Fading are shown.

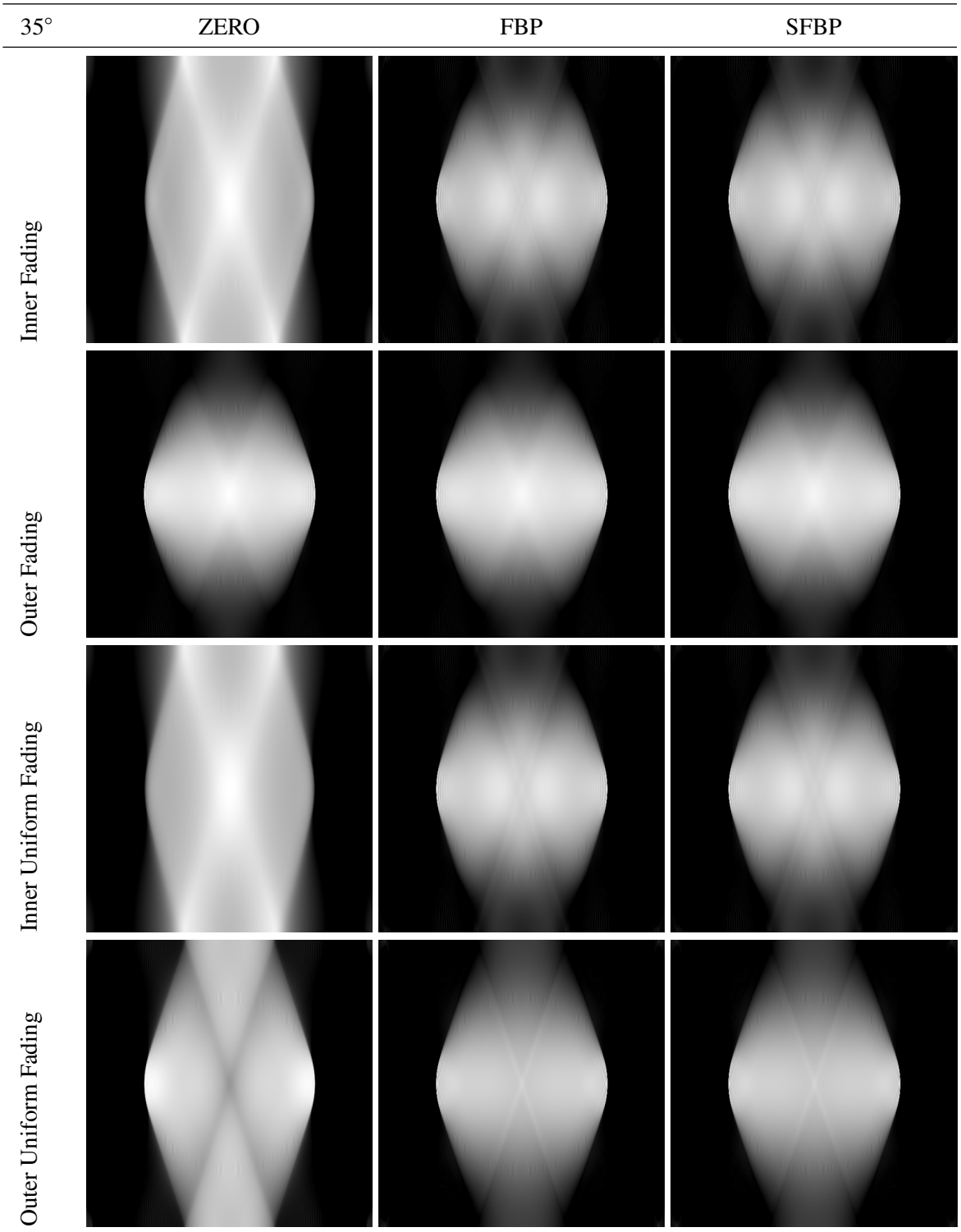

Figure 4.9: Reconstruction of the ball of size 512 x 512 without presence of noise, limited angle $\Phi = 35°$. Reconstructions for the initial values ZERO, FBP and SFBP, and Curvelet tilings Inner Fading, Outer Fading, Inner Uniform Fading, Outer Uniform Fading are shown.

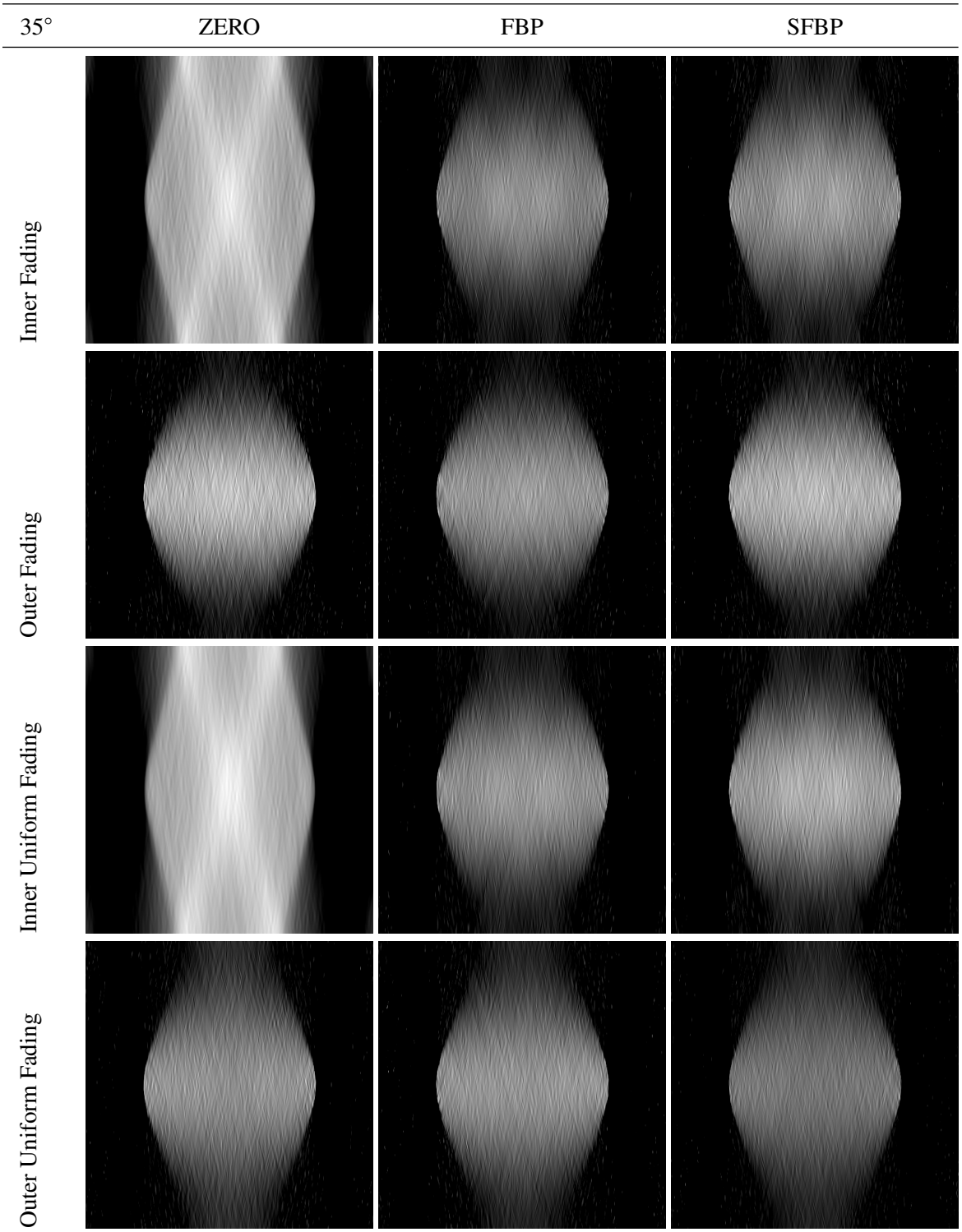

Figure 4.10: Reconstruction of the ball of size 512 x 512 without presence of noise, limited angle $\Phi = 35°$. Reconstructions for the initial values ZERO, FBP and SFBP, and Curvelet tilings Inner Fading, Outer Fading, Inner Uniform Fading, Outer Uniform Fading are shown.

Algorithm 1: Iterative soft-thresholding in limited angle tomography

Data: $c_0 \leftarrow$ initial Value according to Section 4.3;
$\tau_{(j,k,l)} \leftarrow$ thresholding sequence according to (1.29) or (1.30);
$s_{min}, s_{max} \leftarrow$ minimal and maximal step length according to (1.28);
$s \leftarrow$ initial step length with $s_{min} \leq s \leq s_{max}$;
$n_{max} \leftarrow$ maximum number of iterations;

Result: Reconstruction f_{rec}

```
while n < n_max do
    c^{n+1} ← S_{τ^n}(c^n − sK*(Kc^n − y^δ));
    y_rec^{n+1} ← Kc^{n+1};
    if ||y^δ − y_rec^{n+1}|| < ||y^δ − y_rec^n|| then
        n ← n + 1;
        s ← min{(1/f) s, s_max};
    else
        if s = s_min then
            n ← n + 1;
        else
            s ← max{f s, s_min};
        end
    end
end
f_rec ← T c^{n_max};
```

4.6 Conclusion: Comparison of the different parameter values

We conclude this chapter by discussing and evaluating the presented numerical results. We divide this into three topics:

- What influence has the choice of the curvelet tiling?
- What influence has the choice of the initial value?
- What has to be considered in the presence of noise?

The Curvelet tiling

As we can see in Figures 4.3 to 4.10 the choice of the used tiling has a great influence on the numerical result. The Inner and Inner Uniform Fading clearly showed the most artifacts. This may be a result of the broken admissibility conditions. Both Uniform Fadings lead to a slightly blurred image. This can nicely be explained by the fewer angular scales in the higher radial scales. Finally, the Outer fading yields a sharp image with very reduced artifacts. The computational time for the Inner and Outer Fading is increased in comparison to both Uniform Fadings. All in all we favor the Outer Fading or the Outer Uniform Fading depending on the available computational resources and the desired computational time.

Initial Value

The choice of the initial value has an influence on the numerical results, too. This can be seen best in Figures 4.9 and 4.10 in the case of Inner or Inner Uniform Fading. In case of the Outer or Outer Uniform Fading the initial value is only important in the first iterations. Both the FBP and SFBP lead to acceptable images in very few iterations. The initial value ZERO naturally needs more iterations to produce an acceptable image. Therefore for experiments with a large number of iterations and the use of the Outer or Outer Uniform Fading all three initial values are suitable for both a noise free and noisy situation. If the computational time is of importance and only a small number of iterations is acceptable, the initial value SFBP is preferable. Both initial values FBP and SFBP increase the sensitivity to noise in the first iterations.

All in all the initial value SFBP leads to good results in all of the considered situations and hence, is to be preferred.

Noise sensitivity

As can be seen in Figures 4.4, 4.6, 4.8 and 4.10, the procedure can handle noise very well. The qualitative result is not affected. If the initial values FBP or SFP are used the noise leads to strong artifacts in the initial values, but is removed quickly during the consecutive iterations.

5 Discussion

In the present thesis we elaborate an artifact-free reconstruction method in limited angle tomography. The introduced method is capable of handling noise in the measurement data.

We introduce the mathematical background in Chapter 1. The limited angle Radon transform is used to model the data acquisition process. This transform describes the measurements by integrals over oriented lines. Bundled by angle, these integrals form projections. In limited angle tomography these projections are only available for a limited angular range. The data for angles outside this range is missing. Afterwards, we introduce the curvelet frame. This frame is powerful in representing objects with edges in a sparse way. Curvelets yield an optimally sparse representation for functions that are C^2 except for discontinuities along C^2 curves. This gives rise to consider sparse reconstruction with respect to the curvelet frame. We describe an iterative soft-thresholding algorithm that solves the established minimization problem and finish Chapter 1 by showing three typical artifacts that are present in images reconstructed from limited angle tomographic measurements. In these images only singularities perpendicular to the data acquisition are recoverable. This feature can not be changed. Furthermore, in reconstructed images from limited angle tomographic measurements dark and bright lines are present all over the image. We concentrate on removing this artifact, which is caused by the hard cut-off of the measurement data at the angular boundaries.

Chapter 2 is dedicated to the adaption to the limited angular range. We present three variants to adjust the curvelet transform to the use in limited angle tomography. The basis for these adaptions is that curvelets, which do not subtend the visible wedge, lie in the kernel of the limited angle Radon transform. We introduce the Inner Fading, which concentrates on solely allowing the reconstruction of coefficients that are measured during data acquisition. The Outer Fading, that weights all measurable coefficients by 1 and weights coefficients that are not measurable lower in order to reduce artifacts. Finally, the Uniform Fading, which uses a uniform, scale independent angular range to remove the hard cut-off by smooth fading, is introduced. All the resulting tilings take artifact reduction into account.

In Chapter 3 we elaborate a fast discrete version of the curvelet transform. We improve a minimal, straight forward workflow of the curvelet analysis and synthesis algorithm until we present a fast digital curvelet transform that is suited for the use in limited angle tomographic reconstruction. This improvements include the removal of unnecessarily slow computations of curvelets in Fourier space

and the reduction of the number of coefficients in order to reduce the redundancy of the corresponding curvelet frame. In the end, we compare our implementation to another implementation of the curvelet transform that is not optimized for the use in limited angle tomography.

The final algorithm is then used in Chapter 4 for numerical experiments. It turns out that both the Outer and Outer Uniform Fading show the least artifacts. In addition to that, for low numbers of angular scales the Uniform Fading leads to a lower computational expense but a blurring of the resulting image. We suggest to use the initial value SFBP, a smoothed filtered backprojection of the measurement data, as it leads to the best compromise between computational time and artifact reduction. We see that the method is capable of handling noise: the qualitative results are left unchanged in comparison to the noise-free simulations.

This thesis is based on the curvelet sparse regularization introduced by Jürgen Frikel in [13] and the curvelet transform introduced by Emanuel Candès et al. in [3]. The main contribution of this work is the development of new tilings of the Fourier plane and the implementation of a modified fast digital curvelet transform that uses these tilings. With these modifications the curvelet transform is well suited for the use in limited angle tomography.

For the numerical experiments the iterative soft-thresholding was used. This method can be split up in two steps: first the descent step, followed by a soft-thresholding step. These two steps are independent from each other. We used gradient descent in the present thesis. For a faster convergence in future works also other, higher order methods could be used. The conjugated gradient or the Newton method could be possible candidates. A speed-up of the computational time would be of great benefit for the applicability of this method.

Appendix

Short introduction to Frames

In this section we will give a brief introduction to frames, following the definitions in [5]. Frames are a mathematic tool to represent elements of a vector space with the use of a known dictionary $\{f_k\}_{k\in I}$ for some index set I. We already know such a tool from basic linear algebra: bases. But the conditions to a basis are very restrictive: A sequence $\{e_k\}_{k=1}^m$, in the vector space V is called a basis of V if the following two condition are satisfied:

$$\begin{aligned} &\text{i)} \quad V = \operatorname{span}\{e_k\}_{k=1}^m, \\ &\text{ii)} \quad \{e_k\}_{k=1}^m \text{ is linearly independent.} \end{aligned} \tag{.1}$$

The first condition seems very natural, as we want to represent every element of the considered vector space. This condition will also be required in the context of frames. The second condition claims linear independence of the elements $\{e_k\}_{k=1}^m$. This is a very strict condition, but it leads to some nice features, like the unique representation of elements $v \in V$, i.e. there exist unique scalar coefficients $\{c_k\}_{k=1}^m$ such that

$$v = \sum_{k=1}^{m} c_k e_k. \tag{.2}$$

Although this feature is desirable, the linear independence makes it very hard (or even impossible) to satisfy extra conditions, like in our case the later Curvelet definition. Therefore Condition (.1ii) is dropped in the context of frames. This leads to the following definition for finite sets $\{f_k\}_{k\in I}$:

A sequence $\{f_k\}_{k=1}^m$, $m \in \mathbb{N}$ of elements in V is called frame, if

$$V = \operatorname{span}\{f_k\}_{k=1}^m. \tag{.3}$$

With this definition one can think of frames as a kind of overcomplete basis, a basis to which additional elements are added. Of course this is not always true. The set $\{f_k\}_{k\in I}$ does not have to contain an actual basis.

The definition (.3) can be generalized by the following definition, assuming not only finite, but also countable index sets I:

A family of elements $\{f_k\}_{k\in I}$ in V is a frame for V if there exist constants $A, B > 0$ such that

$$A\|f\|^2 \leq \sum_{k\in I} |\langle f, f_k\rangle|^2 \leq B\|f\|^2, \ \forall f \in V. \tag{.4}$$

The proof of the equivalence of (.3) and (.4) for finite index sets I can be found in [5, Corollary 1.1.3].

Now that we have defined frames, we want to give some further definitions and features.

Definition: The numbers A, B in Definition (.4) are called *frame bounds*. As obviously for A, B also $A/2, 2B$ are frame bounds, they are not unique. Therefore the *optimal lower* and *optimal upper frame bounds*, $\inf_{\{\text{A is lower frame bound}\}} A$ respectively $\sup_{\{\text{B is lower frame bound}\}} B$, are defined.

If the optimal upper and lower frame bounds coincide, i.e.

$$A\|f\|^2 = \sum_{k\in I} |\langle f, f_k\rangle|^2, \ \forall f \in V. \tag{.5}$$

a frame is called *tight*.

List of Figures

Bibliography

[1] Bredies, K. and D. Lorenz: *Linear convergence of iterative soft-thresholding*. Journal of Fourier Analysis and Applications, 14(5):813–837, 2008.

[2] Candes, E., L. Demanet, D. Donoho and L. Ying: *Fast discrete curvelet transforms*. Multiscale modeling and simulation, 5(3):861–899, 2006.

[3] Candes, E. and D. Donoho: *Curvelets: A surprisingly effective nonadaptive representation for objects with edges*. Techn. Rep., DTIC Document, 2000.

[4] Candes, E. and D. Donoho: *New tight frames of curvelets and optimal representations of objects with piecewise C^2 singularities*. Communications on pure and applied mathematics, 57(2):219–266, 2004.

[5] Christensen, O.: *An introduction to frames and Riesz bases*. birkhauser, 2003.

[6] Daubechies, I.: *Ten lectures on wavelets*. Philadelphia, PA:SIAM, 1992.

[7] Daubechies, I., M. Defrise and C. De Mol: *An iterative thresholding algorithm for linear inverse problems with a sparsity constraint*. Communications on pure and applied mathematics, 57(11):1413–1457, 2004.

[8] Davison, M.: *The ill-conditioned nature of the limited angle tomography problem*. SIAM Journal on Applied Mathematics, pp. 428–448, 1983.

[9] Do, M. and M. Vetterli: *The contourlet transform: an efficient directional multiresolution image representation*. Image Processing, IEEE Transactions on, 14(12):2091–2106, 2005.

[10] Donoho, D.: *Wedgelets: Nearly minimax estimation of edges*. The Annals of Statistics, 27(3):859–897, 1999.

[11] Epstein, C.: *Introduction to the mathematics of medical imaging*. 2007.

[12] Frikel, J.: *Reconstructions in limited angle x-ray tomography: Characterization of classical reconstructions and adapted curvelet sparse regularization*. PhD thesis, Technische Universität München, 2012.

[13] Frikel, J.: *Sparse regularization in limited angle tomography*. Appl. Comput. Harmon. Anal., 34:117–141, (2013).

[14] Griesse, R. and D. Lorenz: *A semismooth Newton method for Tikhonov functionals with sparsity constraints*. Inverse Problems, 24:035007, 2008.

[15] Hörmander, L.: *Linear partial differential operators*, vol. 1963. Springer Berlin, 1963.

[16] Le Pennec, E. and S. Mallat: *Sparse geometric image representations with bandelets*. Image Processing, IEEE Transactions on, 14(4):423–438, 2005.

[17] Ma, J. and G. Plonka: *The curvelet transform*. Signal Processing Magazine, IEEE, 27(2):118–133, 2010.

[18] Mallat, S.: *A wavelet tour of signal processing*. Academic Pr, 1999.

[19] Radon, J.: *On the determination of functions from their integral values along certain manifolds*. Medical Imaging, IEEE Transactions on, 5(4):170–176, 1986.